

1 **Influence of salt-related mechanical layering on the seismic potential of**  
2 **active faults: Insights from the southwestern Valencia Trough (W**  
3 **Mediterranean)**

4  
5 Martin-Rojas, Iván<sup>1</sup>

6 Ramos, Adrià<sup>2,1</sup>

7 De Ruig, Menno<sup>2</sup>

8 Medina-Cascales, Iván<sup>1</sup>

9 Santamaría-Pérez, Eva<sup>1</sup>

10 Alfaro, Pedro<sup>1</sup>

11  
12 1 Dpto. de Ciencias de la Tierra y del Medio Ambiente, Universidad de Alicante,  
13 Campus San Vicente s/n, 03690, San Vicente del Raspeig, Alicante.

14 [ivan.martin@ua.es](mailto:ivan.martin@ua.es)

15 2. Departament de Botànica i Geologia, Universitat de València, 46010 Burjassot,  
16 Valencia, Spain

17 3. Lithologic, 2582 LD The Hague, The Netherlands. lithologic.mail@gmail.com

18 Corresponding author: Martin-Rojas, Iván

19 Dpto. de Ciencias de la Tierra y del Medio Ambiente, Universidad de Alicante,  
20 Campus San Vicente s/n, 03690, San Vicente del Raspeig, Alicante.

21 [ivan.martin@ua.es](mailto:ivan.martin@ua.es)

22

23

24 **Short summary**

25 This study investigates the main active faults located within the southwestern  
26 Valencia Trough, an offshore region east of the Spanish coast. Utilizing subsurface  
27 data, we identify and characterize the 3D geometry of several of these faults for the  
28 first time. Given that active faults pose a significant natural hazard owing to their  
29 potential to generate earthquakes, we also assess the seismic potential of the faults  
30 within the southwestern Valencia Trough.

31

32 **ABSTRACT**

33

34 We present a structural and seismotectonic analysis of active faults in the  
35 southwestern Valencia Trough (western Mediterranean) on the basis of subsurface  
36 datasets. In our study, we identify and characterise three major active faults: the  
37 Cullera Fault, with long-term slip rates that vary over time between  $0.15 \pm 0.1$  mm/yr  
38 and  $0.4 \pm 0.1$  mm/yr; the oblique Albufera Fault, with a long-term slip rate of  $0.2 \pm$   
39  $0.1$  mm/yr; and the normal Valencia Fault.

40 The seismogenic character of the southwestern Valencia Trough is controlled by a  
41 mechanically weak layer consisting of Triassic evaporites. This weak layer induces  
42 partial-to-complete decoupling between the suprasalt and subsalt successions,  
43 leading to two distinct mechanisms driving fault displacement: tectonic activity and  
44 salt withdrawal. A quantitative evolutionary analysis of the Cullera Fault reveals that  
45 these two mechanisms occur alternately over time.

46 The presence of a mechanically weak layer has implications for seismicity.  
47 Earthquakes can nucleate within both sub- and suprasalt successions, with total or  
48 partial decoupling influencing rupture propagation. We discuss how these two  
49 scenarios lead to different earthquakes and thus impact the seismic hazard of a  
50 region. Empirical source-scaling relationships, which are commonly used to  
51 estimate the seismogenic potential of active faults, generally assume a  
52 homogeneous seismogenic crust. To address this limitation, we propose a  
53 methodological approach based on the use of the aspect ratio. Using this method,  
54 the maximum magnitudes for suprasalt ruptures are 5.8-6.4, 5.4-6.2, and 5.1-5.9 for  
55 the Cullera, Valencia, and Albufera faults, respectively. These values are 11-25%  
56 lower than those obtained by considering the rupture of the entire seismogenic  
57 crust. Our findings highlight the need to incorporate stratigraphic mechanical  
58 layering into seismic hazard assessments, particularly in salt-influenced tectonic  
59 settings.

60

## 61 **1. Introduction**

62 Seismic hazard analyses are often performed by scaling relationships. These  
63 relationships are regressions in which the seismogenic potential of active faults is  
64 derived from geometric parameters of the fault, such as the potential fault rupture  
65 length or area (Stirling et al., 2013). Pioneering works on scaling relationships began  
66 in the 1970s (Kanamori & Anderson, 1975; Geller, 1976). The regressions of Wells &  
67 Coppersmith (1994) represent a milestone in the application of scaling  
68 relationships, as they included a very large dataset of historical earthquakes. The  
69 equations proposed by Wells & Coppersmith became a standard for determining  
70 the seismogenic potential of active faults. Subsequently, other scaling relationships  
71 have been proposed, accounting for factors such as the tectonic environment, fault  
72 dip, or seismogenic thickness (Stirling et al., 2002 and 2013; Leonard 2010 and  
73 2014; Huang et al., 2024, among many others).

74 Most scaling relationships employed to evaluate crustal earthquakes correlate the  
75 moment magnitude ( $M_w$ ) with the fault dimensions (length, width, and/or area).  
76 Some of these scaling relationships consider the fault width vs. fault dip growth of  
77 ruptures for large earthquakes, as rupture width is limited by the maximum depth of  
78 the seismogenic crust (Leonard, 2010; Yen and Ma, 2011; Leonard, 2014; Cheng et  
79 al., 2019). Standard relationships include data from hundreds or even thousands of  
80 events. Therefore, the influence in these relationships of potential mechanical  
81 heterogeneities within the seismogenic crust should be implicit. However, because  
82 of the large amount of data, the mean regressions average out the less common  
83 situations, as the presence of a mechanical weak layer. Therefore, as a  
84 consequence of this averaging, the empirical relationships do not permit to  
85 compute the influence of potential heterogeneities within the seismogenic crust.  
86 These heterogeneities could control the vertical propagation of ruptures and,  
87 therefore, the magnitude of earthquakes.

88 Here, we present an analysis of several subsurface datasets, including high-  
89 resolution seismic profiles, from the southwestern Valencia Trough. We identify and  
90 characterise the main active faults in this region, and we carry out a detailed  
91 geometric description. The results of this analysis also emphasize that this region is

92 characterised by a mechanically weak layer within the seismogenic crust. After  
93 mapping the main faults, we apply conventional scaling relationships to evaluate  
94 the potential magnitudes of future earthquakes. We propose a methodological  
95 approach for integrating the effects of mechanically weak layers—such as Triassic  
96 evaporites—into routine seismic hazard assessments, highlighting the need to  
97 refine existing scaling relationships in tectonically complex settings.

## 98 **2. Tectonic setting**

99 The Valencia Trough is an extensional basin located in the western Mediterranean  
100 region (Fig. 1). This basin is the result of polyphase tectonic evolution spanning from  
101 the Triassic to the present day, as it is located between the Betic–Balearic fold-and-  
102 thrust belt to the south, the Iberian Chain to the west, and the Catalan Coastal  
103 Range to the north (De Ruig, 1992; Guimerà & Álvaro, 1990; Maillard & Mauffret,  
104 1999; Roca & Desegaulx, 1992; Roca et al., 2004; Vergés & Fernández, 2012). The  
105 tectonic evolution of the Valencia Trough is also partially influenced by extension  
106 related to the retreat of the Maghrebian–Ligurian Tethys subduction slab (Etheve et  
107 al., 2016; Faccenna et al., 2004; Jolivet & Faccenna, 2000; Maillard & Mauffret, 1999;  
108 Rehault et al., 1984; Roca et al., 1999; Séranne, 1999; van Hinsbergen et al., 2014).

109 The Valencia Trough (Fig. 1) underwent a Mesozoic rifting process related to the  
110 Iberian intraplate rift and the opening of the Western Tethys (Arche and López-  
111 Gómez, 1996; Nebot and Guimerà, 2018; Ramos et al., 2023; Salas et al., 2001). This  
112 process led to the formation of NW–SE and NE–SW high-angle faults offsetting the  
113 pre-Mesozoic basement and to the deposition of a 5–15-km-thick Upper Jurassic-  
114 Lower Cretaceous succession.

115 During the Late Cretaceous, the onset of convergence between Nubia and Eurasia  
116 caused the transition from a Mesozoic extensional tectonic regime to successive  
117 compressional and extensional stages (Roca, 2001; Salas et al., 2001; Vergés and  
118 Sàbat, 1999). From the late Eocene to the Oligocene, the Valencia Trough was  
119 dominated by shortening. Onshore, this episode led to the formation of the  
120 intraplate Iberian Chain and Catalan Coastal Ranges (Gaspar-Escribano et al.,  
121 2004; Geel, 1995; Guimerà and Álvaro, 1990).

122 From the late Oligocene to the middle Miocene, the western Mediterranean region  
123 was subsequently affected by an extensional regime, driven by the complex  
124 interplay between the European–Cenozoic rift system (e.g., Séranne, 1999) and the  
125 rollback of the Maghrebian–Ligurian Tethys slab (Faccenna et al., 2004; van  
126 Hinsbergen et al., 2014). This extensional phase led to the formation of the Liguro-  
127 Provençal and Algerian Basins, as well as the Valencia Trough. However, subsidence  
128 in the southwestern Valencia Trough during this period cannot be accounted for by

129 rifting, due to the limited occurrence of Cenozoic basement extensional faults  
130 (Roca and Guimerà, 1992). Therefore, extension has been interpreted as due to the  
131 collapse of a back-arc transient uplift event (Fang et al., 2021).

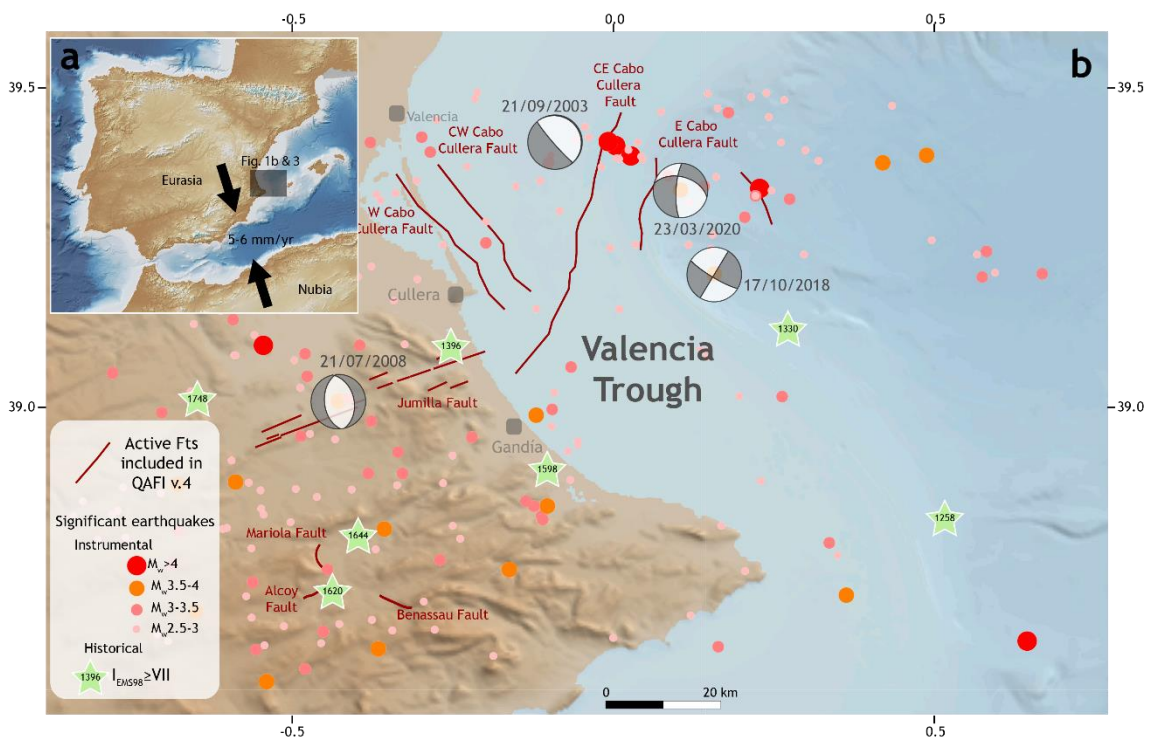
132 The extension in the Valencia Trough occurred immediately before or synchronously  
133 with the formation of the compressional Betic Cordillera. This compressional  
134 deformation is well expressed by a thin-skinned fold-and-thrust system observed in  
135 the Eastern Betic Cordillera (De Ruig, 1995; Sàbat et al., 2011) and in the Balearic  
136 Promontory (Mallorca and Ibiza Islands). At the same time, significant magmatic  
137 activity took place in the area. This magmatism was divided into two phases: (1) late  
138 Oligocene to Serravallian calc-alkaline activity and (2) Tortonian to present alkaline  
139 volcanic activity (Martí et al., 1992).

140 From the Pliocene to the present, the tectonic setting in the Valencia Trough has  
141 been dominated by NE–SW extension, as indicated by focal mechanisms (Stich et  
142 al., 2010) and broad regional global navigation satellite system (GNSS) analyses  
143 (Stich et al., 2006). This extension has been related to thermal subsidence (Roca,  
144 1992, 1996, and 2001; Roca and Guimerà, 1992; Roca et al., 1999a; Gaspar-  
145 Escribano et al., 2004) and has been interpreted as the final stage of an aborted rift  
146 event responsible for the ENE motion of the Balearic promontory (Palano et al.,  
147 2015). Several normal active faults have been defined in the southwestern Valencia  
148 Trough thus far (Fig. 1): the Western Cabo Cullera Fault, Central–Western Cabo  
149 Cullera Fault, Central–Eastern Cabo Cullera Fault, Eastern Cabo Cullera Fault and  
150 Southwest Columbretes Fault (Perea, 2006). Some of these faults were previously  
151 recognised from vintage seismic lines (Diaz del Rio et al., 1986; Roca, 1992, 1996;  
152 Perea, 2006; Maillard & Mauffret, 2013), but fault traces and geometry were defined  
153 only very approximately. Similarly, the slip rates derived from the displacement of  
154 Plio-Quaternary seismic reflectors observed in the vintage seismic lines present  
155 high uncertainties ( $0.02 \pm 0.01$  mm/yr; Perea, 2006). In the Valencia Trough,  
156 seismicity is characterised by low- to moderate-magnitude events (Fig. 1). The few  
157 available focal mechanisms (Stich et al., 2010; IGN, 2025) indicate a normal–  
158 oblique or strike slip kinematics, although these focal mechanisms present high  
159 uncertainties, mainly because they occur at long distances from seismic stations

160 and are registered with significant azimuthal gaps (González, 2017). According to  
161 the data published by the Spanish Earthquake Catalogue (IGN, 2025), this  
162 seismicity is very shallow, as most of the events are assigned depths of less than 10  
163 km (Fig. 2). However, these data should be taken with caution, as the depths  
164 assigned to these earthquakes present high uncertainties (González, 2017).

165 In the onshore domain located west of the Valencia Trough, only one major active  
166 structure, namely, the Jumilla Fault, has been postulated (García-Mayordomo et al.,  
167 2012), together with other minor active faults (Alcoy, Mariola, and Benasau Faults).  
168 In this onshore area, several significant historical earthquakes have occurred, such  
169 as the 1396 Tavernes ( $I_{EMS98}=VIII-IX$ ), 1620 Alcoy ( $I_{EMS98}=VIII-IX$ ), 1644 Muro ( $I_{EMS98}=V$ )  
170 and 1748 Estubeny ( $I_{EMS98}=IX$ ) earthquakes (Martínez Solares and Mezcuca, 2002;  
171 IGN, 2025; Buforn et al., 2105; Buforn & Udías, 2022).

172



173

174 Fig. 1. a. Location of the Valencia Trough. Convergence vectors between Nubia and  
175 Eurasia are after DeMets et al., 1994; McClusky et al., 2003; Nocquet, 2012;  
176 Nocquet & Calais, 2003; Pérez-Peña et al., 2010; Serpelloni et al., 2007; Stich et al.,  
177 2006. b. Seismotectonic map of the southwestern Valencia Trough and surrounding

178 areas. Fault traces from Quaternary-Active Faults of Iberia database (García-  
179 Mayordomo et al., 2012)

180

181



182

183 Fig 2. Seismicity of  $M_w > 2.5$  in the southwestern Valencia Trough shallower than 20  
184 km since 1950 from the *Instituto Geográfico Nacional* database (IGN, 2025). a.  
185 Distribution of the depth of seismicity. The horizontal axis represents distance along  
186 the southwestern Valencia Trough in a SW-NE direction (from the SW shoreline to  
187 the NE Mediterranean Sea). b. Energy (from magnitude) and depth histogram. In  
188 both graphics events with 0 km of the assigned depth are not represented (fixed  
189 depth).

### 190 3. Data

191 The interpretation of the offshore area is based on mainly 2D multichannel seismic  
192 reflection data calibrated with well data (Fig. 3). The central part of the study area is  
193 covered by a high-quality seismic survey acquired by Fugro-Geoteam with the RV  
194 Geo Baltic, processed by Robertson Research International Ltd. in 2002. The survey  
195 consists of 30 seismic sections with an average length of 90 km (totalling  
196 approximately 2,800 km). They are oriented WNW–ESE and NNE–SSW, with  
197 maximum spacings of 13 km and 6 km, respectively. The details regarding the  
198 acquisition and processing parameters can be found in Cameselle & Urgeles (2017).  
199 Most of the area affected by Plio-Quaternary faulting nearer to the coast is covered  
200 only by vintage 2D seismic lines from the late 1970s, acquired by various operators,  
201 which are publicly available upon request in the Instituto Geológico y Minero de  
202 España (IGME-CSIC) (<http://info.igme.es/sigeof/>). More than 100 of these seismic  
203 lines, with a total line length of approximately 2,500 km, were selected for mapping;  
204 although the quality of these lines varies from moderate to poor, the high-density  
205 grid spacing (varying from 1 to 3.5 km) allows fault mapping with reasonable  
206 confidence. The seismic interpretation was performed in two-way travel time (TWT)  
207 by using Move software (by Petex). The seismic dataset was converted to depths  
208 using velocity data derived from the Expanded Spread Profile (ESP) 7 (Pascal et al.,  
209 1992; Torné et al., 1992). A second-order polynomial trend was applied to establish  
210 time–depth relationships, ensuring strong correlation with the well data, similar to  
211 the methodologies of Fang et al. (2021).

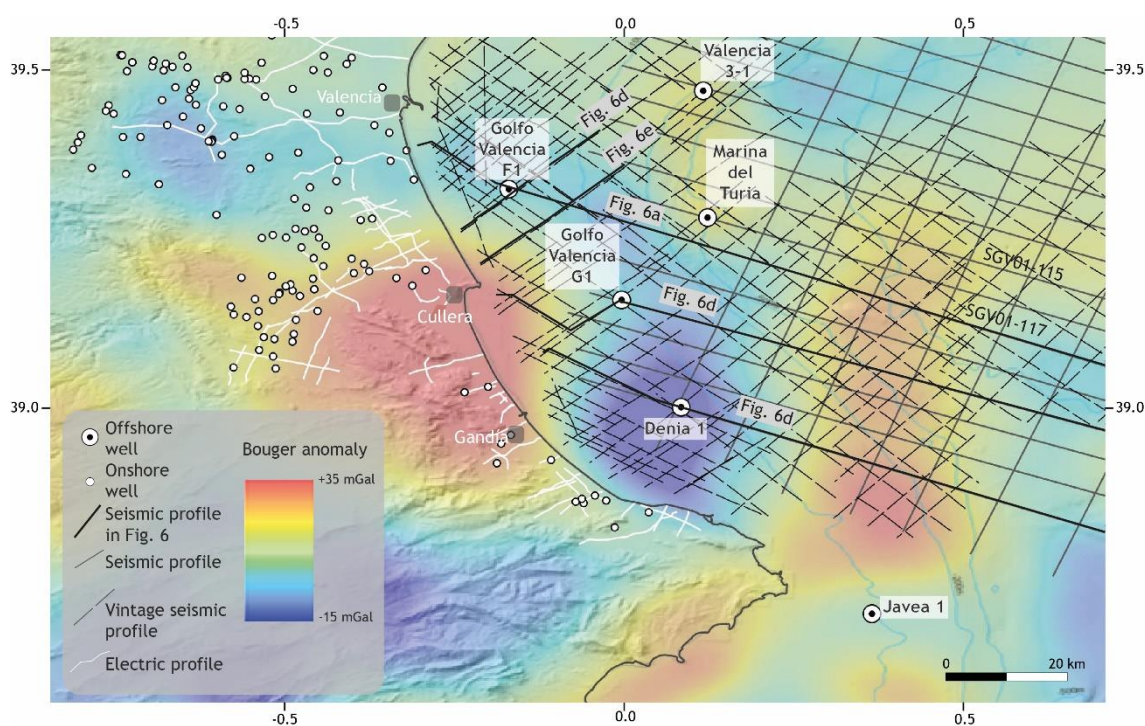
212 The interpretation of seismic horizons is calibrated by 9 offshore petroleum  
213 exploration wells, all of which penetrate the entire Neogene section and whose  
214 bottoms are in Mesozoic rocks. Original well reports, log data (lithology, dipmeter,  
215 gamma–ray, sonic and resistivity data) and palaeontological data (from cuttings and  
216 sidewall cores) were retrieved from the IGME-CSIC archive  
217 (<https://info.igme.es/hidrocarburos/>). Well-to-seismic ties were established by  
218 integrating the sonic logs and using synthetic seismograms from end-of-well  
219 reports. Palaeontological analyses and range charts from the original well reports

220 were reviewed and adapted to the Mediterranean biozonation of Lirer et al. (2019) to  
221 obtain approximate absolute ages for the seismic horizons.

222 No seismic data were available for the onshore area of southern Valencia and only  
223 two deep exploration wells were drilled (Jaraco-1 and Perenchiza-1). However,  
224 stratigraphic information is available from 95 hydrogeological wells in the Valencia  
225 coastal plain, as are vertical electric sounding (VES) profiles acquired for  
226 hydrogeological surveys. The data are publicly available in the online IGME-CSIC  
227 databases IRYDA, BD Puntos Agua 2.0 and Sistema de Información Documental  
228 (SID) (accessible through <https://info.igme.es/catalogo/>).

229 In areas with poor seismic coverage, structural mapping was aided by regional  
230 Bouguer gravity anomalies processed with a Butterworth high-pass filter with a 1-  
231 degree cut-off frequency to highlight short-wavelength features of the data (by  
232 Getech, 2015).

233



234

235 Fig. 3. Geophysical dataset used in this work. Filtered Bouguer anomaly data after  
236 Getech (2015). The location is shown in figure 1.

237

#### 238 **4. Stratigraphy**

239 The general stratigraphic arrangement of the southwestern Valencia Trough (Fig. 4)  
240 consists of a rigid Palaeozoic–Middle Triassic basement overlain by a 1.5–7-km  
241 Upper Triassic–Quaternary stratigraphic cover. Here we present a new detailed  
242 stratigraphic framework for the late Miocene–Quaternary of the southern Valencia  
243 Trough. The definition of the pre-Neogene stratigraphic units presented in this work  
244 is based on mainly previous literature and our analysis of well data, as well as  
245 outcrops in the mainland for the most recent sediments.

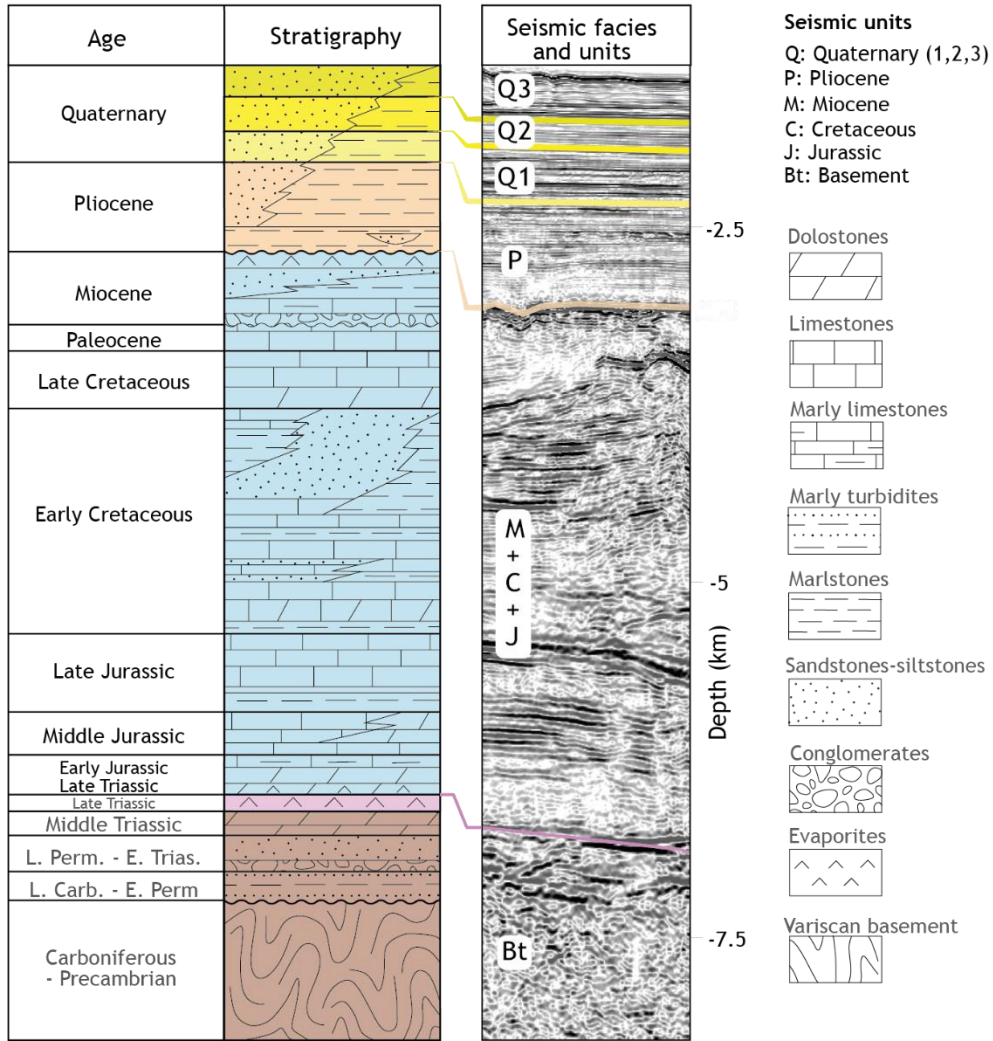
246 The Upper Triassic succession (Fig. 4) consists of evaporites, shales and dolomites  
247 (Keuper Facies) (Vargas et al., 2009). The Upper Triassic deposits are overlain by  
248 Early Jurassic to Late Cretaceous carbonates and marls (Salas et al., 2001). erosive,  
249 angular unconformity that is directly overlain by Neogene deposits. The Cenozoic  
250 succession starts with a transition from continental clastic sediments to marine  
251 platform carbonates, ending with a deposit formed by progradational terrigenous  
252 shelf-talus sediments (Arche et al., 2010; Clavell and Berástegui, 1991; Etheve et  
253 al., 2018; Lanaja, 1987; Maillard et al., 1992; Ribó et al., 2016b, 2016a; Roca and  
254 Desegaulx, 1992; Soler et al., 1986). The Neogene succession onshore of the  
255 southwestern Valencia Trough (Fig. 4) mostly consists of middle–late Miocene  
256 continental to marginal marine deposits, including limestones, marls and coarse-  
257 grained detrital sediments. The top of the Miocene series is an erosional  
258 unconformity (Messinian Erosion Surface (MES) (Stampfli & Höcker, 1989; Lofi et al.,  
259 2011; Cameselle et al., 2014).

260 Pliocene–recent sediments form a large prograding shelf complex with prominent  
261 clinofolds visible in seismic data, which downlap onto the MES. Prominent  
262 undulations on slope foresets are visible on most seismic lines and are interpreted  
263 as sediment waves (Ribó et al., 2015). In the offshore wells, the stratigraphic  
264 succession consists of an overall shallowing-upward series of thick grey claystones  
265 with calcareous interbeds at the base, grading upwards into sandstones and shell  
266 beds at the top. No unconformities have been identified in the entire sequence,  
267 except for erosional gullies and canyons at the shelf edge. The Plio-Quaternary  
268 sequence reaches a maximum thickness of approximately 3000 m.

269 To determine the Plio-Quaternary depositional history and slip rate of major faults,  
270 six seismic horizons have been mapped and dated with palaeontological data from  
271 offshore wells, via the biostratigraphic scheme of Lirer et al. (2019). Starting from  
272 the Messinian unconformity at 5.3 Ma, seismic markers have been dated at 3.8 Ma  
273 (LO of *G. margaritae*), 3.3 Ma (FO *G. bononiensis*), 2.6 Ma (LCO *G. obliquus*) and 2.0  
274 Ma (FO *G. truncatulinoides*). As no samples were collected from any of the offshore  
275 wells above the lower-middle Pleistocene interval, an additional marker  
276 (approximately 1.0 Ma) was picked halfway through the 2.0 Ma marker and seabed  
277 (0 Ma), assuming a constant sedimentation rate.

278 Isopach maps (Fig. 5) were produced for the intervals of Pliocene (MES to 2.6 Ma  
279 marker) and Pleistocene–recent (2.6 Ma marker to the seabed), revealing a  
280 significant shift in the location of the depocentre. The Pliocene depocentre is  
281 located very close to the southern coast near Denia, attaining a maximum thickness  
282 of approximately 1500 m, whereas the Pleistocene depocentre has prograded ca.  
283 20 km to the NNW, reaching a thickness of more than 1750 m. The western  
284 shoreward edge of both the Pliocene and Pleistocene depocentres is controlled by  
285 very large NNW–SSE-trending normal faults (see below).

286 The described stratigraphic architecture indicates significant mechanical layering  
287 in the southwestern Valencia Trough. A rigid basement is overlain by a mechanically  
288 weak layer represented by the Upper Triassic Keuper Facies. Above this interval, a  
289 rigid Mesozoic carbonate succession is present, followed by a semirigid layer  
290 composed of primarily detrital deposits.



291

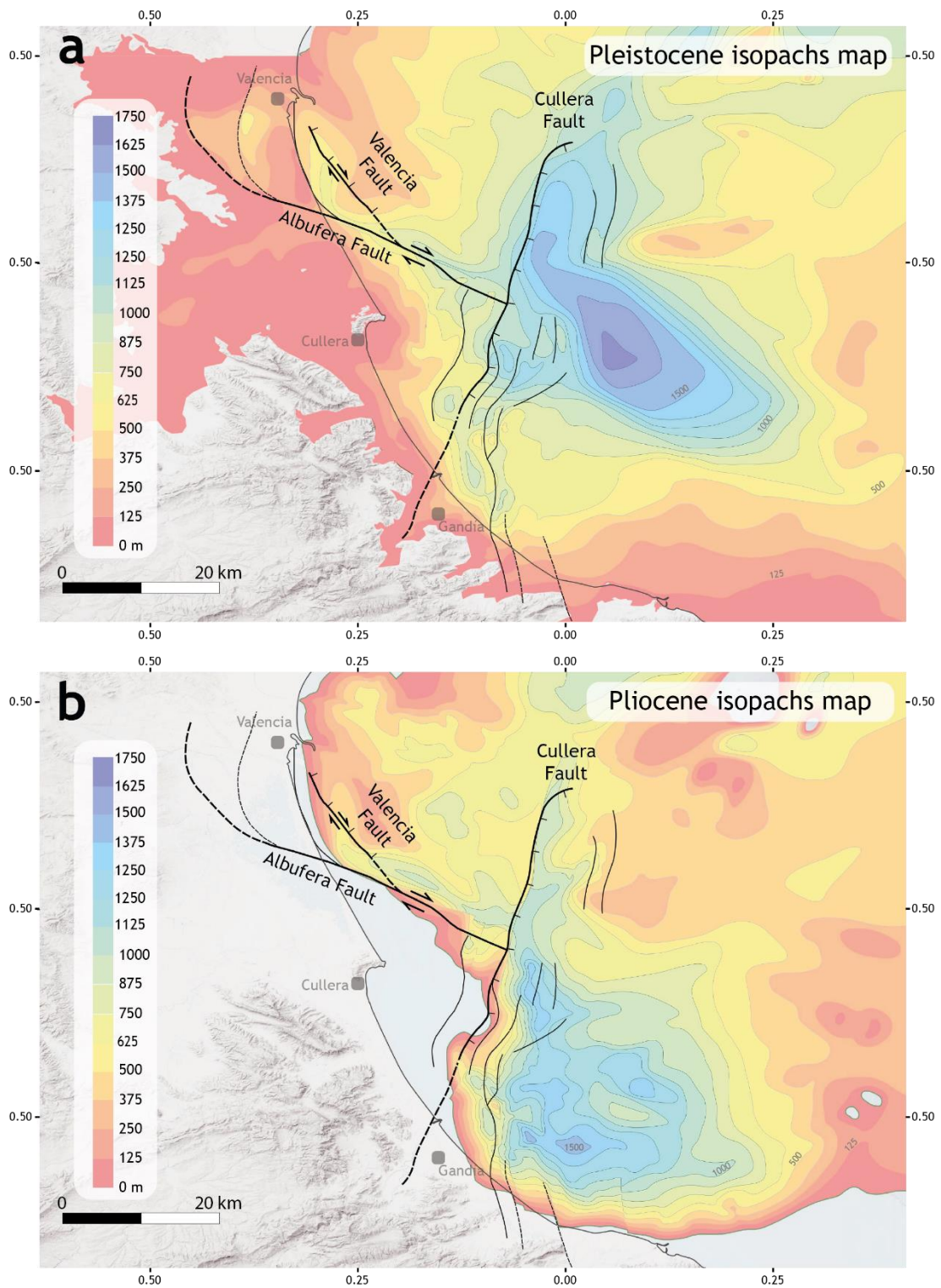
292

293

294

295

Figure 4: Chronostratigraphic diagram of the southwestern Valencia Trough. Note that the depth scale shows maximum thicknesses of the units.



296

297 Figure 5. Isopach maps of the southwestern Valencia Trough for the Pleistocene (a)  
 298 and Pliocene (b). The traces of the active faults are also depicted. Fault traces

299 represent the horizontal projection of the direction line of the fault plane, located  
300 midway between the intersection line of the top-of-the-Pliocene horizon and the  
301 top-of-the-Quaternary horizon. Fault traces are derived primarily from their position  
302 on seismic profiles, supplemented by isopach maps and observed thickness  
303 variations in stratigraphic units, as indicated by the available wells. Dashed lines  
304 show interpreted traces. Modified from Ramos et al. (2025).

## 305 **5. Main active faults in the southwestern Valencia Trough**

306 In this section, we describe the main structural features of the southwestern  
307 Valencia Trough after the analysis of gravity data and isopach maps obtained from  
308 the subsurface dataset (seismic lines, wells and VES) (Figs. 3 and 5).

309 The filtered Bouguer anomaly map (Fig. 3) reveals a positive anomaly in the central  
310 part of the study area, referred to as the Cullera anomaly. This positive anomaly is  
311 surrounded by a region exhibiting a negative anomaly, particularly in the offshore  
312 area located east of Cullera. We interpret this pattern of anomalies to be because  
313 of mass excess associated with a basement high (Cullera positive anomaly)  
314 surrounded by a region with greater sedimentary cover (negative anomaly). This  
315 interpretation is further supported by the isopach maps derived from interpretation  
316 of the subsurface data (Fig. 5). The negative gravity anomaly correlates with an  
317 abrupt increase in the thickness of both the Pliocene and Quaternary sedimentary  
318 successions. Furthermore, the transitions in both the gravity anomaly and  
319 sedimentary thickness correspond to the positions of the main faults observed in  
320 the seismic dataset (see below). On the basis of this evidence, we propose that the  
321 southwestern Valencia Trough is structurally characterised by the presence of three  
322 major faults offsetting the basement and significantly influencing the stratigraphic  
323 evolution of the area. These three major faults are: the Cullera Fault, the Valencia  
324 Fault and the Albufera Fault (Fig. 5).

325 The structural configuration of the southwestern Valencia Trough is also influenced  
326 by the presence of Upper Triassic evaporites and shales at the base of the Mesozoic  
327 sedimentary cover. Major faults offsetting the Mesozoic–Quaternary succession  
328 present a listric geometry with a main ramp that flattens out in the Upper Triassic  
329 salt layer (Fig. 6). These geometries have been interpreted as evidence of a strain  
330 partitioning between the suprasalt and the subsalt successions (Etheve et al., 2016;  
331 Fang et al., 2021; Muñoz Martín & Vicente Muñoz, 1988). According to these  
332 interpretations, the Upper Triassic is a mechanically weak layer that induces  
333 tectonic decoupling within the seismogenic crust of the southwestern Valencia  
334 Trough. As a result, the deformation style of the suprasalt succession (cover) differs  
335 significantly from that of the subsalt succession (basement) (Etheve et al., 2018;

336 Fang et al., 2021; Ramos et al., 2023, 2025; Roma et al., 2018). The main difference  
337 is that normal faults present a listric geometry in the cover, while these faults are  
338 planar within the basement (see below).

339 The analysis of the seismic reflection profiles (Fig. 6) reveals three fault types: i)  
340 faults restricted to the subsalt basement; ii) faults restricted to the suprasalt cover;  
341 and iii) faults cutting through the sedimentary cover, basement and salt layer.

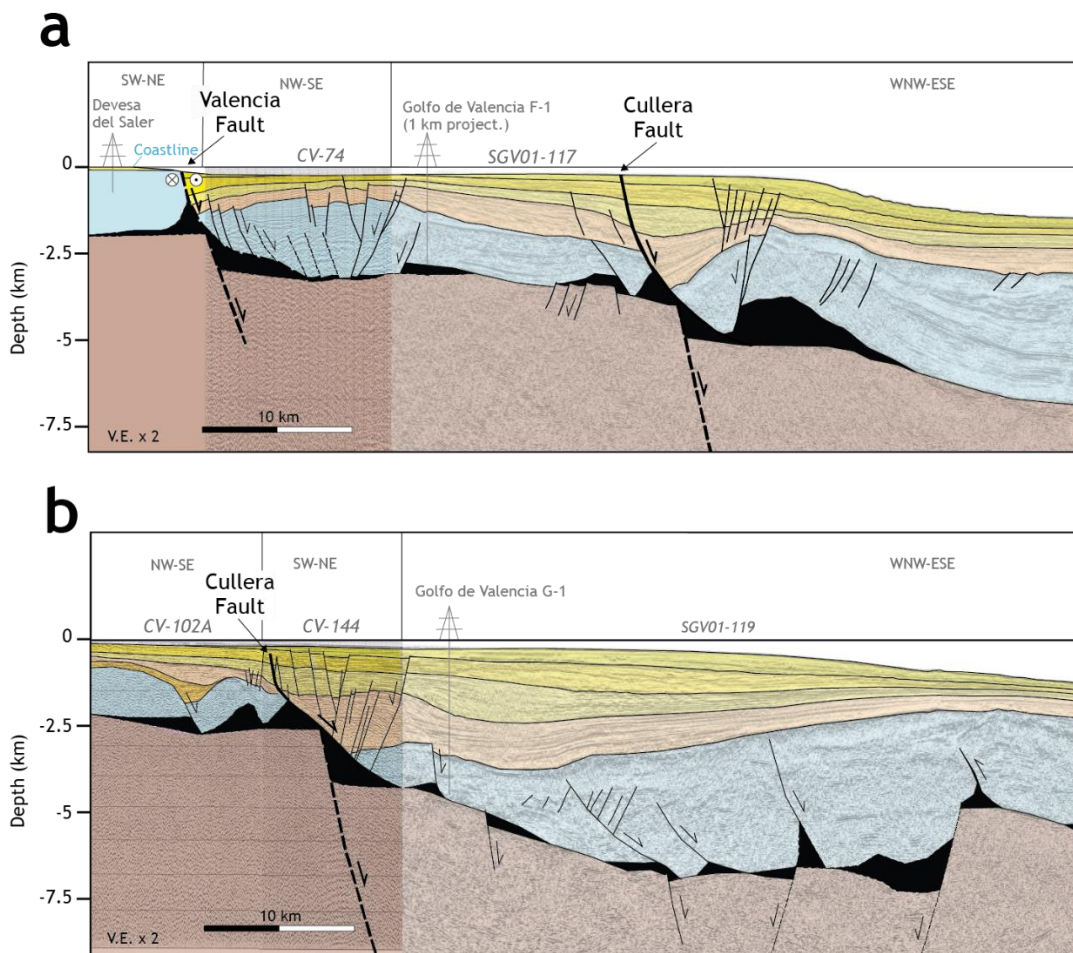
342

343

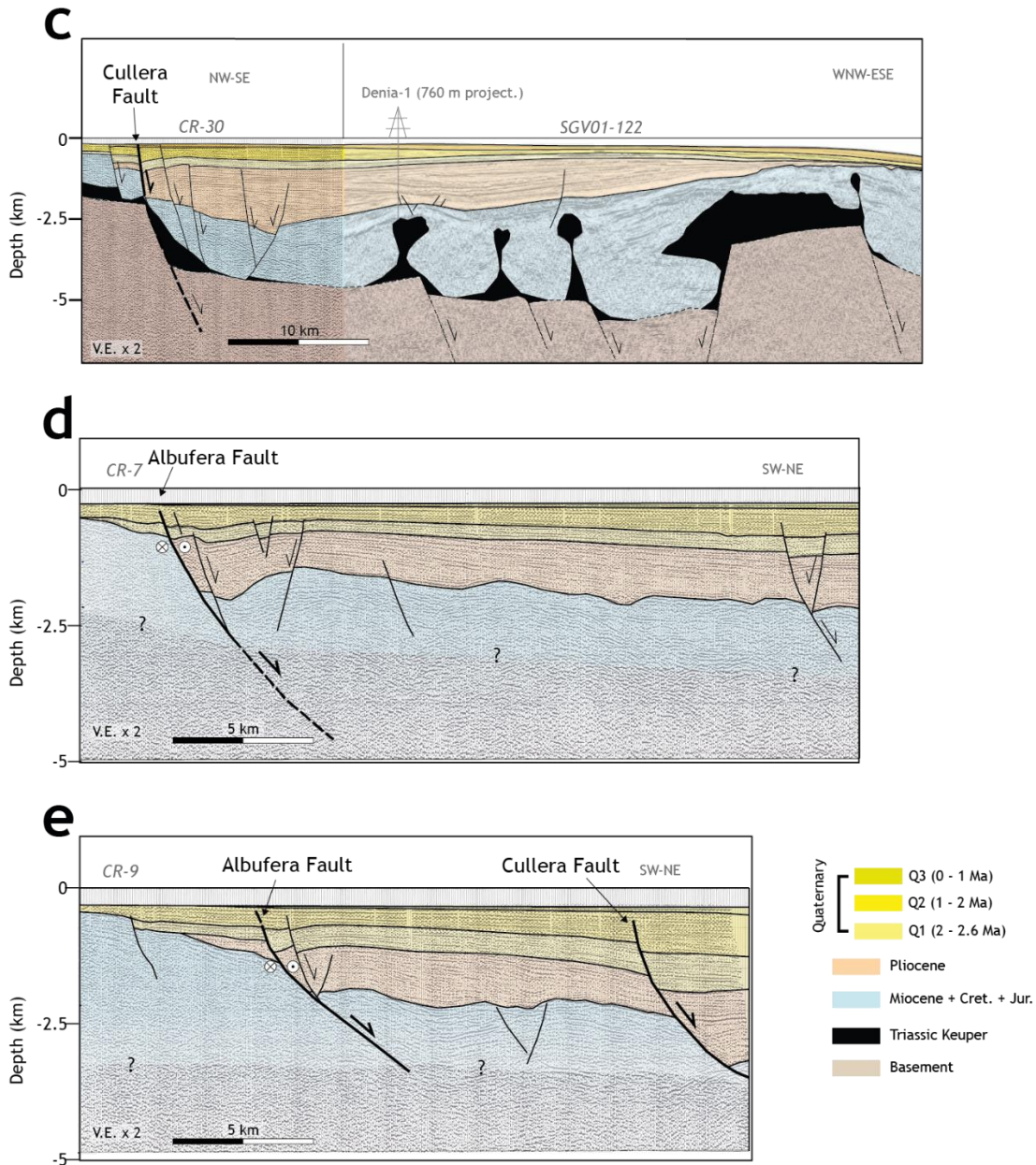
344

345

346



347



348

349 Fig. 6. Interpreted sections derived from onshore cross-sections (a) and the offshore  
 350 2D seismic profiles (a-e). Sections in a-d depict the structure of both the supra- and  
 351 subsalt successions, while in sections in d-e only the suprasalt structure is  
 352 represented. See Fig. 3 for the location. a-c sections after Ramos et al., 2025. Unit  
 353 colours are as those in Fig. 4 (except for the Triassic unit). Note the x2 vertical  
 354 exaggeration of all the sections.

355

356 **5.1 Cullera Fault**

357 The Cullera Fault is the longest along-strike fault in the region, spans approximately  
358 59 km, and has the highest cumulative offset, with more than 1800 m of vertical  
359 displacement at the top of the Messinian horizon (Figs. 5 and 6).

360 The along-section geometry of the fault across the suprasalt succession is well  
361 imaged in the seismic reflection dataset (Fig. 6). The Cullera Fault is a normal, NNE–  
362 SSW-trending fault that dips highly towards the east. The fault offsets the entire  
363 suprasalt cover, including the 1 Ma horizon. Owing to the low resolution of the  
364 available bathymetric data, it is not possible to confirm whether the fault offsets the  
365 seafloor. The Cullera Fault displaces the top of the basement horizon, indicating  
366 that this fault involves both subsalt and suprasalt successions.

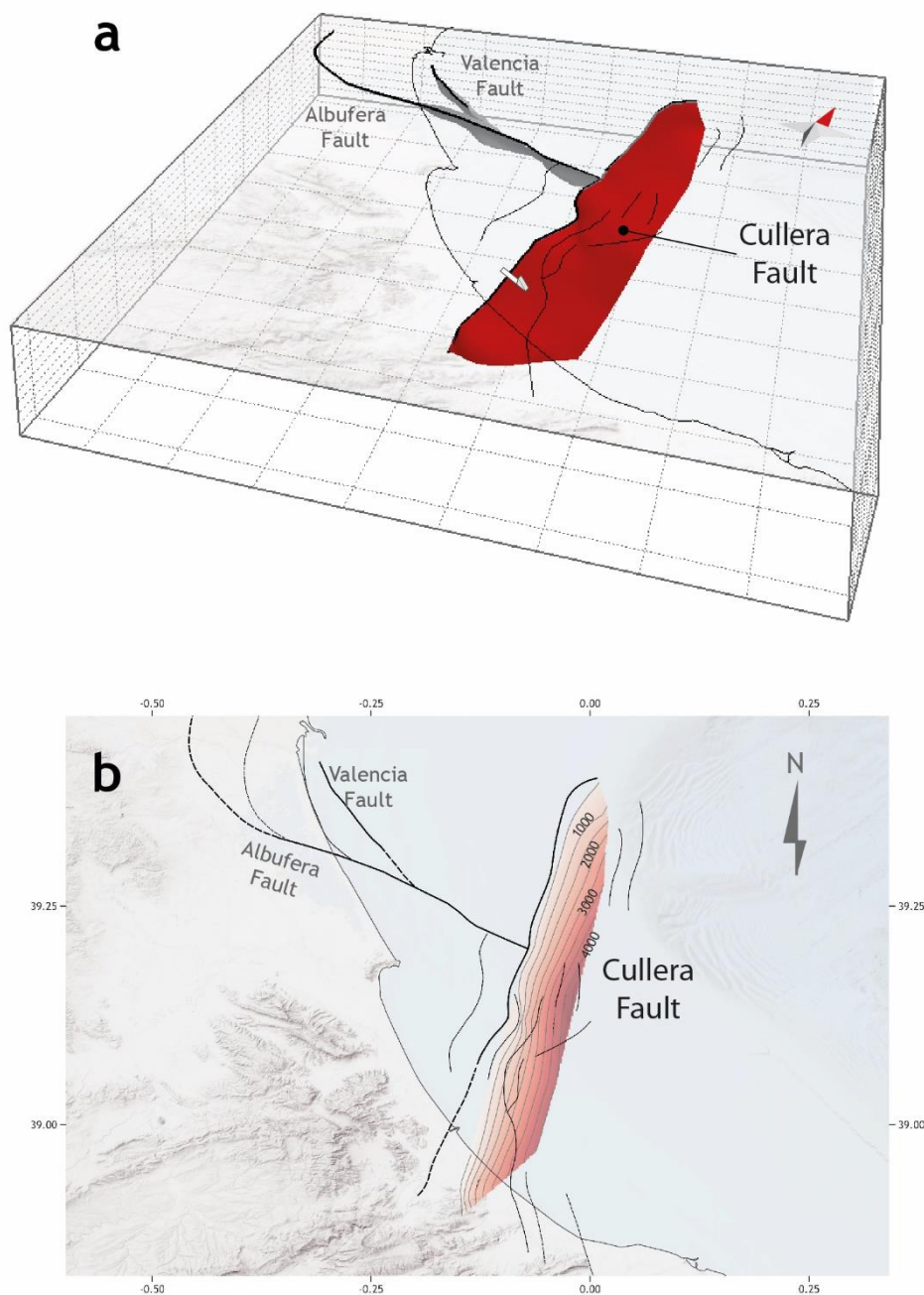
367 Within the basement, the Cullera Fault is poorly imaged in seismic profiles.  
368 Nevertheless, the available data suggest that it is a planar fault (Fig. 6). This is also  
369 supported by the absence of significant tilting of the basement-top horizon.

370 In contrast, the geometry of the Cullera Fault in the sedimentary cover is  
371 heterogeneous. In the northern area (Fig. 6), the part of the Cullera Fault offsetting  
372 the cover exhibits a listric geometry, which is responsible for the development of a  
373 rollover structure in the hanging wall (Fig. 6). Southwards, the listric geometry and  
374 related rollover fold becomes less pronounced (Fig. 6).

375 To better constrain the geometry of the Cullera Fault, we constructed a structural  
376 map of the fault by integrating fault traces identified in the seismic reflection dataset  
377 with isopach maps (Fig. 7). Additionally, a 3D model of the Cullera Fault, along with  
378 the two other major faults, was generated following a 2½D construction approach,  
379 integrating interpreted seismic profiles via interpolation. We employed the ordinary  
380 kriging algorithm implemented in MOVE software, a methodology consistent with  
381 previous approaches applied to analogous structures (Ramos et al., 2020). Analysis  
382 of the reconstructed 3D fault indicates that the surface area of the Cullera Fault  
383 offsetting the sedimentary cover is approximately 360 km<sup>2</sup>.

384

385



386

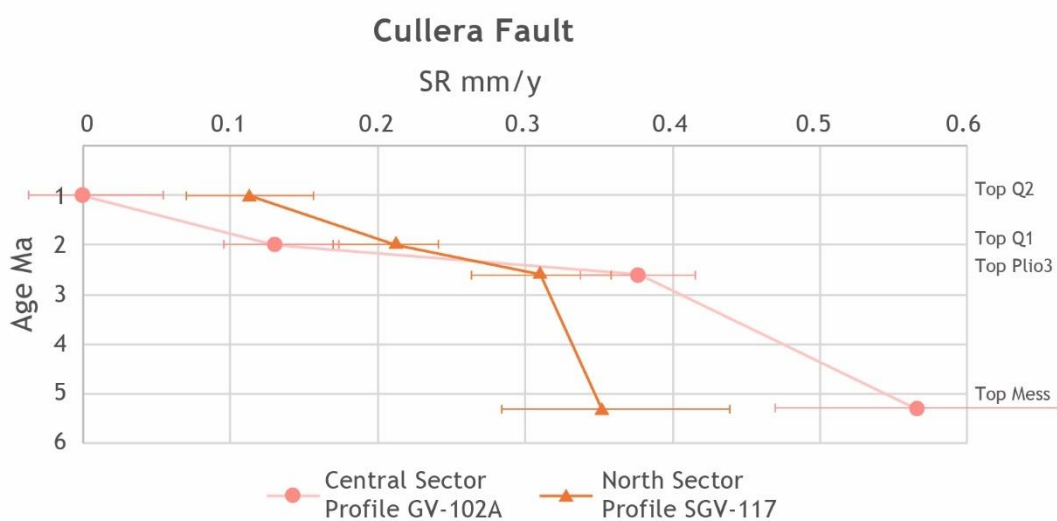
387 Figure 7. 3D model (a) and structural map (b) of the Cullera Fault (red surface).  
 388 Squares in figure 7a represent 10 km x 10 km. Note the red arrow pointing to the  
 389 north in figure 7a.

390

391 Several minor normal faults have developed in the hanging wall of the Cullera Fault  
 392 (Figs. 5). These faults displace only the suprasalt succession without affecting the  
 393 underlying subsalt units. In previous studies (e.g., Perea 2006; Roca 1992), distinct  
 394 names were assigned to these faults, such as the Western Cabo Cullera Fault,

395 Central Cabo Cullera Fault, and Eastern Cabo Cullera Fault. However, the improved  
 396 resolution and quality of the new seismic dataset enable a more detailed  
 397 characterisation of these tectonic structures, allowing for a reassessment of their  
 398 nomenclature and role. We interpret these minor faults to be part of the damage  
 399 zone associated with the main Cullera Fault.

400 The quality of the seismic dataset allows for an analysis of the slip rate of the Cullera  
 401 Fault. This analysis is approximate, because of the resolution of the seismic profiles,  
 402 the uncertainties in the recognition of the markers in the hanging wall and footwall,  
 403 and the age of these markers. Net slip rates were obtained for the Top-Messinian,  
 404 Top Pliocene, Top-Q1, and Top-Q2 horizons, with assigned ages of 5.3 Ma, 2.6 Ma, 2  
 405 Ma, and 1 Ma, respectively (Fig. 8). The slip rates for the Cullera Fault seem to have  
 406 decreased over time, as the calculation yielded mean slip rates of  $0.40 \pm 0.1$  mm/y  
 407 for the Pliocene and  $0.15 \pm 0.1$  mm/y for the Quaternary. This slip rate reduction  
 408 could be the consequence of a change in the regional tectonic regime in the  
 409 complex tectonic cadre of the western Mediterranean region. However, as the  
 410 Cullera Fault is a salt-influenced structure, different mechanisms control fault  
 411 offset. We discuss in section 6 the potential reasons behind this observed decrease  
 412 in slip rate. In any case, we cannot dismiss that at least part of this apparent in-time  
 413 evolution could be an artefact related to the epistemic uncertainties mentioned  
 414 above.



415

416 Figure 8. Long term slip rates (SR) for the Cullera Fault derived from the seismic  
417 profiles for the Top Messinian, Top Plio3, Top Q1, and Top Q2 horizons. The pink line  
418 and dots represent SR for the central sector of the fault. The orange line and triangles  
419 indicate SR for the north sector of the fault. The slip rates seem to decrease in time,  
420 from  $0.40 \pm 0.1$  mm/y for the Pliocene to  $0.15 \pm 0.1$  mm/y for the Quaternary. Error  
421 bars are estimated on the basis of uncertainties in the recognition of the markers  
422 and their ages.

423

## 424 **5.2. Albufera Fault**

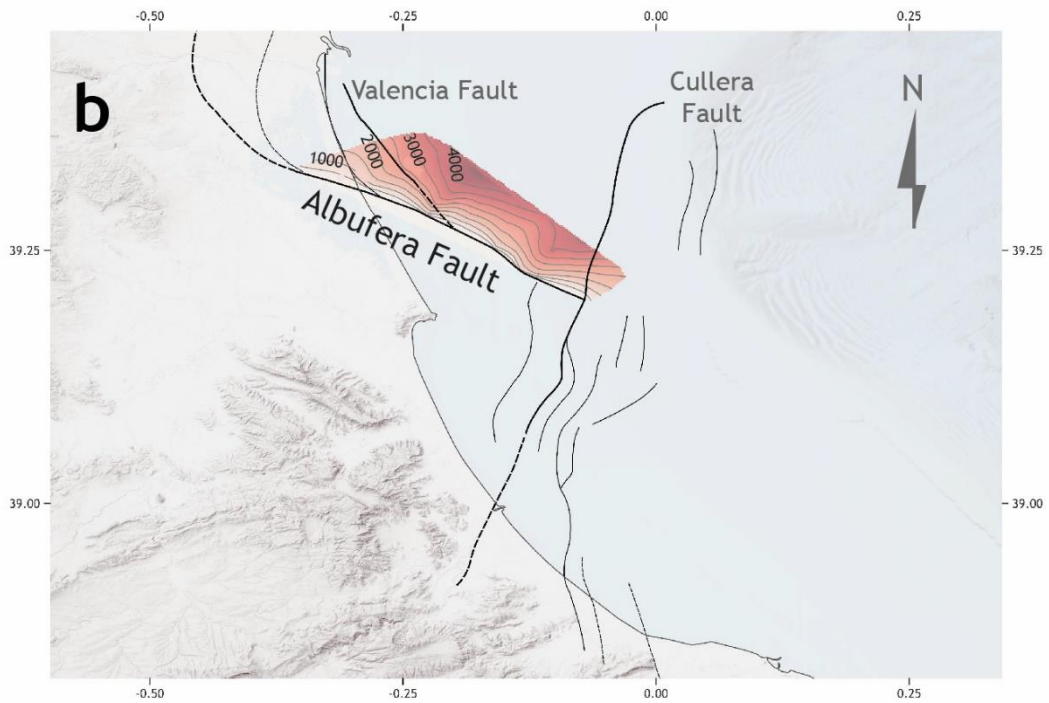
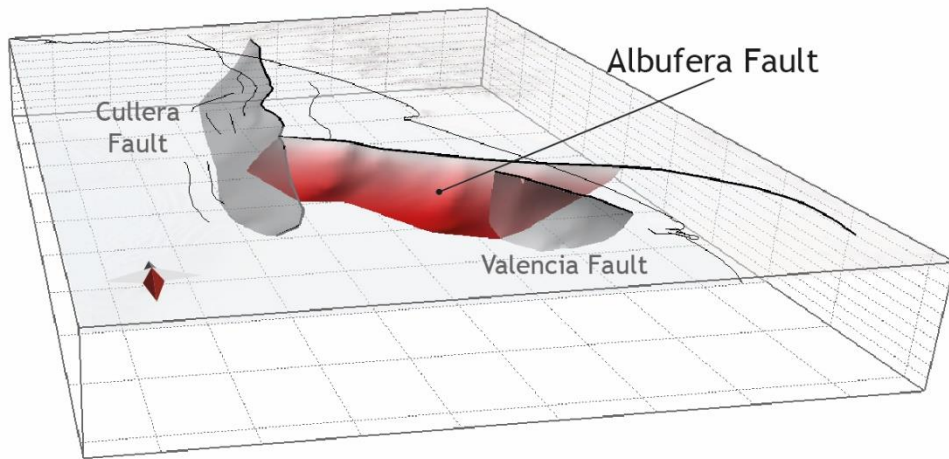
425 The Albufera Fault (Figs. 5 and 6) is a newly defined active structure in the  
426 southwestern Valencia Trough. This NW–SE striking fault extends approximately 55  
427 km and presents an oblique kinematic, with a major strike slip component and a  
428 minor normal displacement (see below). The Albufera Fault exhibits a maximum  
429 vertical offset of 1000 m for the Top-Messinian horizon. This would imply a long-term  
430 vertical slip rate of  $0.2 \pm 0.1$  mm/y. The fault offsets both the supra- and subsalt  
431 successions (Figs. 5 and 6). The Albufera Fault is visible only in the vintage seismic  
432 reflection dataset, where it presents a low dip and a listric geometry.

433 The Albufera Fault appears to offset the entire suprasalt cover, including the 1 Ma  
434 horizon. As with other faults in the region, the low resolution of the available  
435 bathymetric data prevents us from determining whether this fault offsets the  
436 seabed. Nevertheless, high-resolution seismic profiles from the offshore shelf  
437 analysed by previous authors indicate seabed offsets caused by secondary normal  
438 faults likely associated with the Albufera Fault (Díaz de Ríó et al., 1986; Albarracín  
439 et al., 2013).

440 The available seismic dataset reveals a normal kinematic component for the  
441 Albufera Fault. However, mapping of small-scale fault traces in upper Pleistocene–  
442 recent sediments (interval between the seabed and the 1.8 Ma horizon) reveals that  
443 these faults are oblique to the main trend of the Albufera Fault, forming an en  
444 echelon pattern in map view, which suggests that the Plio-Quaternary reactivation  
445 of the main fault has a significant right-lateral strike-slip component. This dextral

446 component is consistent with the regional ENE–WSW direction of Plio-Quaternary  
447 extension in the southwestern Valencia Trough and kinematically consistent with  
448 NNW–SSE trending normal faults. The fault influences the Plio-Quaternary  
449 sedimentary infill of the southwestern Valencia Trough (Fig. 5). The isopach maps  
450 reveal that the Pliocene and Quaternary succession significantly increased in the  
451 hanging wall relative to the footwall. The listric geometry of the Albufera Fault is  
452 responsible for the development of a rollover anticline in the hanging wall (Fig. 6).  
453 This anticline is likely accentuated by the palaeoshelf edge of the late Tortonian–  
454 early Messinian shelf, which is located in the central part of the rollover structure.  
455 To further constrain the geometry of the Albufera Fault, a structural map and a 3D  
456 model of the fault was constructed (Fig. 9). Analysis of the reconstructed 3D fault  
457 surface indicates that the fault encompasses an area of approximately 560 km<sup>2</sup>.

**a**



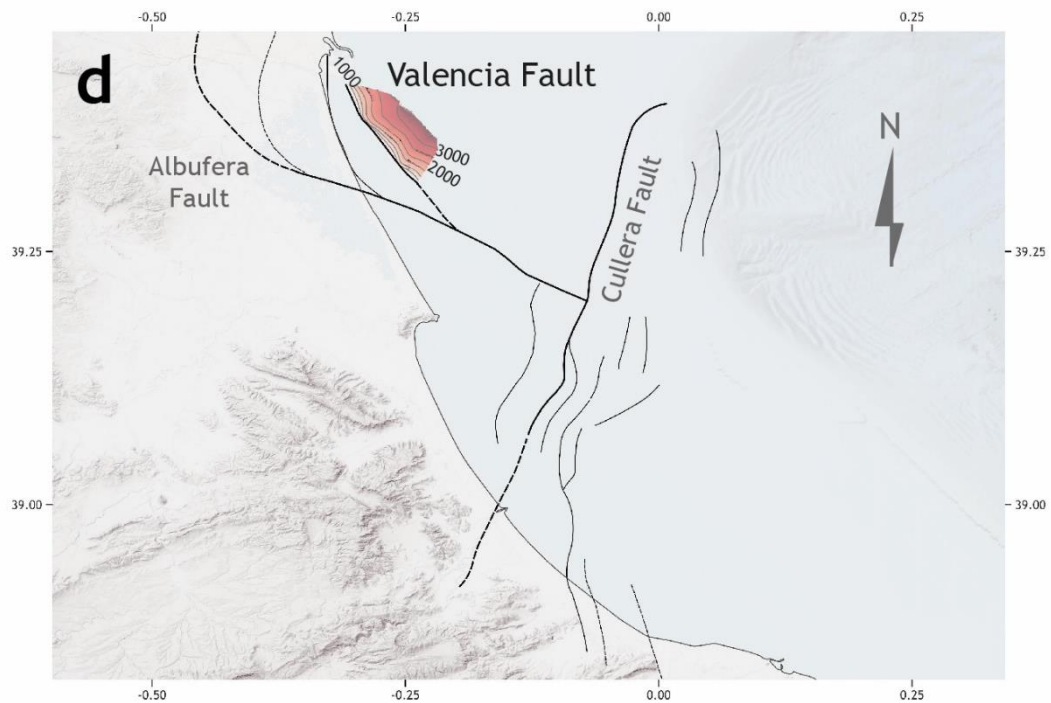
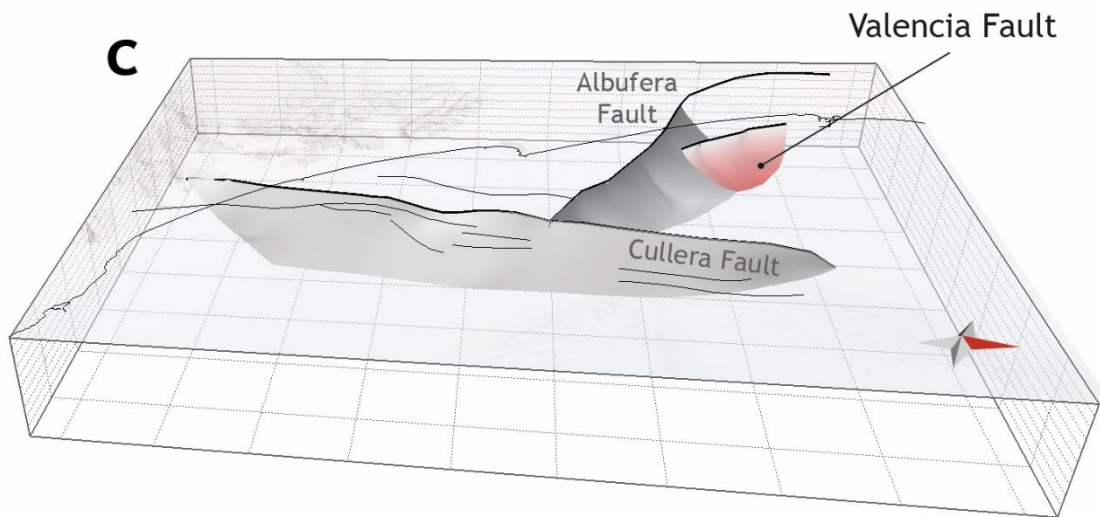
458

459

460

461

462



463

464 Figure 9. 3D model and structural map of the Albufera Fault (a and b) and the  
 465 Valencia Fault (c and d). Squares in the 3D models represent 10 km x 10 km boxes.  
 466 Note the red arrow pointing to the north in figures 9a and 9c.

467

468

469 **5.3 Valencia Fault**

470 In this section, we describe the Valencia Fault (Figs. 5 and 6). This structure could  
471 correspond to the Western Cabo Cullera Fault (*sensu* Perea, 2006). The Valencia  
472 Fault presents a length of approximately 20 km and has a significant impact on the  
473 distribution of Quaternary depocentres. The Valencia Fault present a normal  
474 component, as it vertically displaces both the supra- and subsalt successions (see  
475 below) (Figs. 5 and 6). However, taking into account the general structural  
476 arrangement of the southwestern Valencia Trough, we postulate that the Valencia  
477 Fault presents also a strike-slip component.

478 This NNW–SSE trending, steeply dipping fault is imaged primarily in the vintage  
479 seismic reflection dataset, where it exhibits a listric geometry, at least in the portion  
480 offsetting the suprasalt succession (Fig. 6). The Valencia Fault vertically offsets the  
481 entire suprasalt cover, including the 1 Ma horizon. However, owing to the low  
482 resolution of the available bathymetric data, it is not possible to determine whether  
483 this fault offsets the seabed. The Valencia Fault also displaces vertically the top of  
484 the basement horizon, indicating that this structure involves both subsalt and  
485 suprasalt successions. Within the basement, the Valencia Fault is not well-imaged  
486 in the seismic profiles, but the absence of tilting in the basement-top horizon  
487 suggests that it is a planar fault (Fig. 6). The Valencia Fault and its secondary strands  
488 very likely continue onshore below the City of Valencia. The lack of onshore seismic  
489 data hampers the mapping of these fault strands, but their presence can be inferred  
490 from the abrupt Plio-Quaternary thickness changes observed in water wells and  
491 vertical electric sounding profiles.

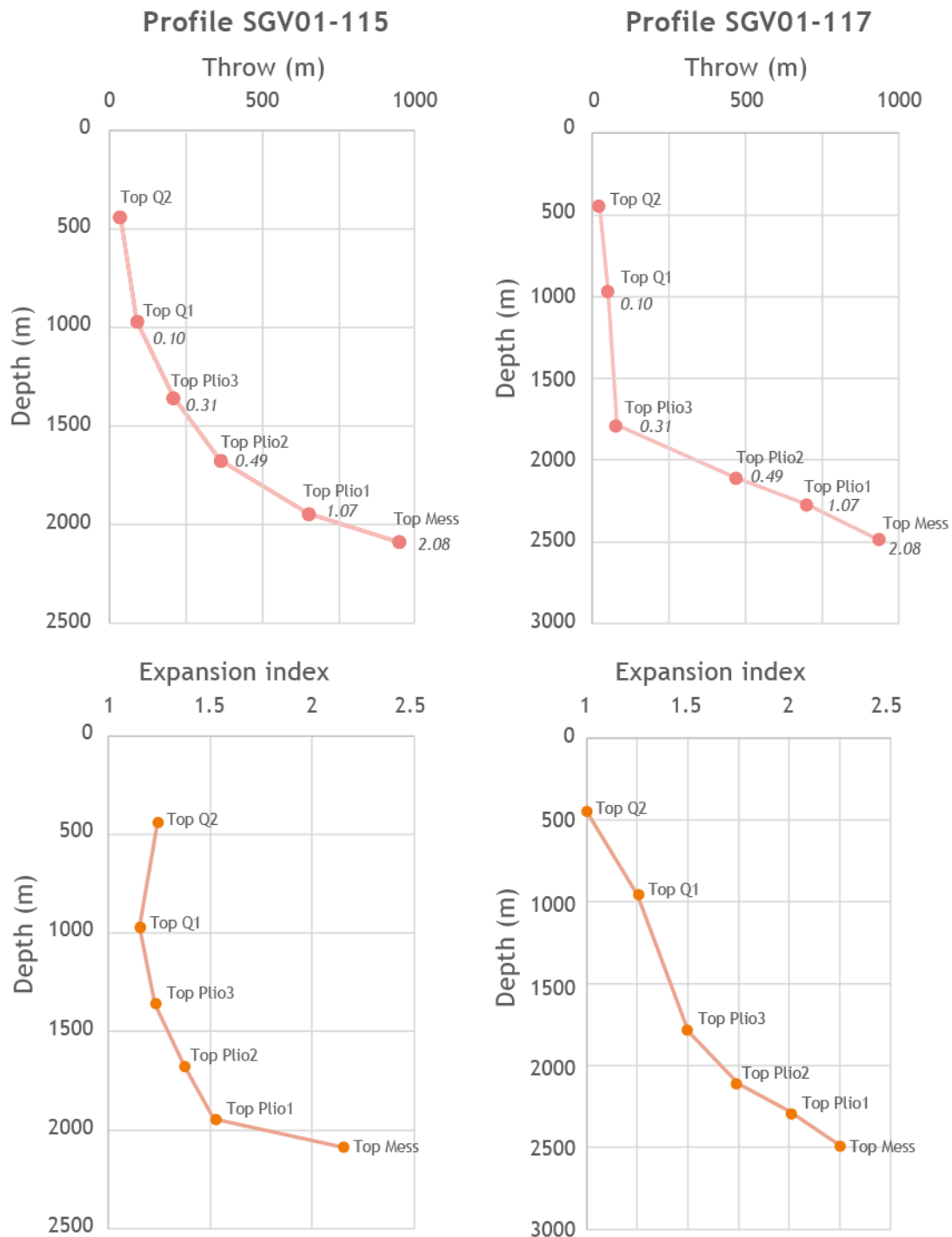
492 To further constrain the geometry of the Valencia Fault, a structural map and a 3D  
493 model of the fault was constructed (Fig. 9). Analysis of the reconstructed 3D fault  
494 surface indicates that the fault encompasses an area of approximately 208 km<sup>2</sup>.

495

496 **6. Evolutionary growth of the Cullera Fault: interplay between tectonics and**  
497 **salt withdrawal.**

498 This section aims to provide further insights into the evolution of the active faults in  
499 the southwestern Valencia Trough. The low resolution of the vintage seismic dataset  
500 limits the ability to perform a detailed analysis only for the Cullera Fault. To analyse  
501 recent along-dip variations in throw, we constructed throw-depth plots (T-z plots)  
502 for the post-Messinian markers (Fig. 10). These plots provide insights into the  
503 evolutionary growth of the fault (Mansfield and Cartwright, 1996; Hongxing and  
504 Anderson, 2007). The quality of the available seismic reflection dataset allows this  
505 analysis to be performed on two seismic profiles located in the northern part of the  
506 fault, where the listric geometry is well-developed (LINES SGV01-115 and SGV01-  
507 117; Figs. 3 and 6).

508 We computed T-z plots for six suprasalt horizons: Top-Messinian, Top Plio1, Top  
509 Plio2, Top Plio3, Top Q1, and Top Q2 (Fig. 10). The T-z plots for the Cullera Fault reveal  
510 a general increase in the throw and throw gradient with depth. We postulate that the  
511 increase observed in the throw is the result the differing ages of the horizons, older  
512 horizons show greater offset because they have been displaced over a longer time  
513 interval. As regards throw gradients, the data indicate two distinct portions: (i) the  
514 lower portion, with higher throw gradients, includes horizons from the Top Messinian  
515 to the Top Pliocene; (ii) the upper portion, with lower throw gradients, comprises the  
516 Quaternary horizons. This distinction is particularly pronounced in the southern  
517 seismic line (line SGV01-117, Fig. 6). Here, the throw gradient decreases, from 2.38–  
518 2.98 in the lower portion to 0.22–0.10 in the upper portion.



519

520 Figure 10. Throw depth (T-z) and expansion index plots for the Cullera Fault  
 521 computed from profiles SGV01-115 and SGV01-117. The numbers within the T-z  
 522 plots indicate the throw gradient for the corresponding interval. The T-z plots reveal  
 523 an increase in the throw and throw gradient, with a higher throw gradient for the Top  
 524 Messinian–Top Pliocene interval and a lower throw gradient for the Quaternary  
 525 interval.

526 The Cullera Fault significantly influences the Plio-Quaternary sedimentary infill of  
527 the southwestern Valencia Trough. Isopach maps indicate a marked increase in the  
528 thickness of both Pliocene and Quaternary successions in the hanging wall with  
529 respect to the footwall (Fig. 5). To quantify this relationship, we computed the  
530 expansion index (Thorsen, 1963; Rouby et al., 2003; Jackson and Rotevatn, 2013) for  
531 the post-Messinian stratigraphic units (Fig. 10). The expansion index consistently  
532 exceeds 1 across all the analysed intervals, indicating a synkinematic deposition in  
533 these units. The Pliocene units exhibit a greater expansion index than the  
534 Quaternary units do, with the difference being particularly pronounced in the  
535 southern seismic line (Fig. 6 LINE SGV01-117).

536 Finally, to shed light on the mechanisms controlling the creation of accommodation  
537 space related to the Cullera Fault, we analyse the tectonic–stratigraphic  
538 arrangement of the hanging wall units. To discuss this point, we compare the  
539 geometries observed in the southwestern Valencia Trough with analogous  
540 stratigraphic geometries in the Danish North Sea, where they have been interpreted  
541 in terms of the evolution of salt-influenced faults (Duffy et al., 2023 and references  
542 therein). In such a setting, two mechanisms create accommodation space: fault  
543 displacement and load-driven salt withdrawal in the hanging-wall. These two  
544 mechanisms can act separately or contemporaneously in time. When the  
545 accommodation space generated by the fault offset exceeds that created by salt  
546 withdrawal, the depocentre axis remains adjacent to the fault. In contrast, when  
547 salt-related accommodation space is dominant, the depocentre migrates away  
548 from the fault (Duffy et al., 2023).

549 In the northern part of the Cullera Fault, where the rollover structure is well  
550 developed (Fig. 6), the position of the Plio-Quaternary depocentre in the hanging-  
551 wall varies along the dip direction. The Pliocene depocentre remains in the  
552 immediate hanging wall of the fault. Therefore, we interpret that, during the  
553 Pliocene, the accommodation space generated by the displacement of the Cullera  
554 Fault exceeded that produced by the accommodation space related to salt  
555 withdrawal. During the deposition of unit Q1, the depocentre migrated basinwards,  
556 suggesting that salt withdrawal-related accommodation space outpaced that

557 related to fault displacement. Finally, during Q2 and Q3, the depocentre axis shifted  
558 towards the fault, indicating that fault displacement-related accommodation space  
559 regained dominance over salt mobility. We postulate that this evolution in the  
560 location of depocentres is related to the mechanisms responsible for the creation  
561 of accommodation space.

562 All the above-described features shed light on the evolution of the salt-influenced  
563 Cullera Fault. As previously discussed, the creation of accommodation space  
564 results from two mechanisms: tectonic offset along the fault and displacement  
565 related to salt withdrawal. Both mechanisms act cumulatively; that is, both  
566 mechanisms produce slip along the Cullera Fault and create accommodation  
567 space. The migration of successive depocentres suggests that, during the Pliocene,  
568 accommodation space related to tectonic offset was greater than that created by  
569 salt withdrawal. As the throw gradient is high ( $\approx 2.4$ ) during this period, we postulate  
570 that both mechanisms were active. During the deposition of Q1 (2.6–2 Ma), the  
571 position of the depocentre suggests that salt mobility became the dominant  
572 mechanism, likely due to a decrease in fault activity, an increase in salt withdrawal,  
573 or both. As throw gradient decreases during this period, we postulate that a  
574 decrease in the fault displacement rate could be the reason for the change in the  
575 main mechanism. Finally, during the rest of the Quaternary (2 Ma to present), fault  
576 displacement-related accommodation space once again exceeded that created by  
577 salt withdrawal. The constant throw gradient observed during this period with  
578 respect to the previous time interval (2.6–2 Ma) suggests that the change in the main  
579 mechanism was due to a reduction in or cessation of salt withdrawal. This  
580 interpretation is further supported by the off-fault geometry of the Q2–Q3  
581 sedimentary bodies, as no significant change in thickness is observed above the salt  
582 withdrawal-related anticlinal crest located east of the Cullera Fault (Fig. 6).

583 Therefore, according to the above exposed, we postulate that, during the Pliocene  
584 and lower Quaternary (up to 2 Ma ago), the offset of the Cullera Fault was produced  
585 by both tectonics and salt withdrawal, being the first mechanism dominant during  
586 the Pliocene and the second during the 2.6–2 Ma time span. From that moment to  
587 the present salt withdrawal ceases (or significantly reduces), and tectonics

588 becomes the only (or very dominant) process. The reduction of salt movement is  
589 possibly due to the complete withdrawal of mobile salt and the formation of a weld  
590 below the hanging wall. This evolution could also explain the slip rate decreases  
591 observed for the Cullera Fault (Fig. 8). A higher slip rate is expected during the  
592 Pliocene, when both tectonics and salt withdrawal were active. Once salt  
593 withdrawal ceases or significantly decreases, a corresponding decrease in the slip  
594 rate is also expected.

595 **7. Influence of mechanical layering on the seismic potential: the case of the**  
596 **southwestern Valencia Trough**

597 The southwestern Valencia Trough has a distinct mechanical stratigraphy  
598 characterised by three layers: a subsalt basement, a weak mechanical layer  
599 composed of Triassic evaporites, and overlain Mesozoic–Quaternary sedimentary  
600 succession. Triassic evaporites are well documented for their ductile behaviour,  
601 which enables them to act as regional detachment layers (e.g., Morley et al., 2003;  
602 Jackson and Hudec, 2005) and inhibits the propagation of faults (e.g., Withjack et  
603 al., 1990; Pascoe et al., 1999; Maurin and Niviere, 2000; Withjack and Callaway,  
604 2000; Richardson et al., 2005; Ford et al., 2007; Kane et al., 2010; Marsh et al., 2010).  
605 Moreover, mechanically weak layers have been shown to induce full or partial  
606 geometric and kinematic decoupling between sub- and supradetachment  
607 successions (e.g., Stewart et al., 1997; Withjack and Callaway, 2000; Ford et al.,  
608 2007; Tvedt et al. 2013). In this section, we focus on the implications of this  
609 mechanical arrangement in terms of how the presence of a weak mechanical layer  
610 influence the vertical propagation of seismic ruptures.

611 In an active region, tectonics are generally the main driving mechanism of fault  
612 displacement. However, in the case of salt-influenced faults, displacement can  
613 also result from salt withdrawal. Our analysis of the evolution of the Cullera Fault  
614 presented in the previous section indicates that the fault offset is related to the  
615 interplay between two mechanisms: tectonic offset along the fault and  
616 displacement related to salt withdrawal. Our analysis also reveals how these two  
617 processes interact with each other. Consequently, in areas with salt-influenced  
618 faults, seismicity can potentially be produced from either mechanism or a  
619 combination of both.

620 In terms of seismic potential, there is a significant difference between a tectonic  
621 earthquake and a salt-withdrawal earthquake. This difference lies in the maximum  
622 potential thickness of the seismogenic layer involved in the rupture. Tectonic stress  
623 affects the entire crust; therefore, strain related to tectonic accumulates both in the  
624 suprasalt and subsalt successions. Consequently, a tectonically driven earthquake  
625 could theoretically rupture the entire seismogenic crust. In contrast, a salt

626 withdrawal-related earthquake would imply offset restricted to the suprasalt  
627 succession, as in this case displacement surface coalesces into the salt layer.  
628 Therefore, in an earthquake restricted to the suprasalt succession, the thickness of  
629 the seismogenic layer is limited by the depth of the mechanically weak layer,  
630 reducing the maximum potential rupture area and, consequently, the seismic  
631 potential. A salt-withdrawal-related earthquake could induce a vertical stress drop  
632 related to salt displacement, potentially triggering displacement in the subsalt  
633 succession and leading to a complex rupture. Similarly, a tectonically driven  
634 earthquake may rupture only the suprasalt succession.

635 Despite the mechanism driving seismicity, the presence of a weak mechanical layer  
636 within the seismogenic crust significantly influences the seismogenic potential of  
637 active faults. We hypothesise that this weak layer could locally hinder the effective  
638 vertical propagation of a rupture, thereby resulting in faults being seismogenically  
639 bounded. Specifically, the total or partial decoupling induced by the weak evaporitic  
640 layer may limit the effective width of the seismogenic layer. This hypothesis is  
641 independent of the weak layer composition; therefore, our hypothesis can be  
642 extended to any region with a similar structural configuration.

643 Significant earthquakes ( $M_w > 6$ ) typically nucleate at depths greater than 5 km.  
644 However, recent events in central Italy and France have demonstrated that very  
645 shallow (2–5 km) earthquakes of moderate magnitude ( $M_w$  5–6) can also occur  
646 (Chiaraluce et al., 2017; Godano et al., 2025; Improta et al., 2019). In the  
647 southwestern Valencia Trough, the thickness of the supra-salt succession is slightly  
648 less than 5 km. Therefore, while the probability of a significant earthquake  
649 nucleating within the supra-salt succession is low, it is not zero. In this section we  
650 evaluate the seismic potential of these (unlikely) supra-salt ruptures. The case of  
651 central Italy could be taken as a geologic and tectonic analogous of the  
652 southwestern Valencia Trough. Central Italy resembles the southwestern Valencia  
653 Trough as both regions are presently dominated by extensional tectonics, and both  
654 are characterised by a pronounced mechanical layering in the upper crust.  
655 Recently, central Italy has undergone high seismicity, including the 1997-1998  
656 Umbria-Marche, 2009 L'Aquila, and 2016-2017 Amatrice-Norcia seismic sequences

657 (Chiaraluce et al., 2003; Valoroso et al., 2013 Chiaraluce et al., 2017; Improta et al.,  
658 2019; Michele et al., 2020). The area of central Italy where these seismic sequences  
659 took place is characterized by a complex geological framework consisting of several  
660 geological domains. Most of this area belongs to the Umbria-Marche fold-and-  
661 thrust belt. This belt consists of a crystalline basement overlain by a 3-8-km-thick  
662 Mesozoic–Quaternary sedimentary cover (Cresta et al., 1989; Centamore et al.,  
663 1992; Menichetti and Coccioni, 2013). The sedimentary Mesozoic succession starts  
664 with a 1.2 km thick salt layer (Anidriti di Burano Formation; Martinis and Pieri, 1964)  
665 acting as a mechanical weak layer. That is, similar to the southwestern Valencia  
666 Trough, the seismogenic crust of central Italy is characterised by the presence of a  
667 mechanically weak layer. As a consequence of thrusting during the Miocene-  
668 Pliocene, this weak layer is vertically repeated in some sectors (Barchi et al., 2021).  
669 Therefore, in central Italy the seismogenic crust includes from one to three weak  
670 layers.

671 Central Italy undergoes extension responsible for normal active faults. These active  
672 normal faults are the seismogenic sources of the seismic sequences occurred in  
673 the last decades (e.g., Boncio et al., 2004; Barchi and Mirabella, 2009), as well as  
674 several historical events (Rovida et al., 2020). Normal active faults in central Italy  
675 present a listric geometry in the sedimentary cover and offset the top of the  
676 basement (Barchi et al., 2021). The 1997-1998 Umbria- Marche and 2016-2017  
677 Amatrice-Norcia seismic sequences nucleated within the suprasalt succession,  
678 including main events (Mw 5-6) with very shallow centroids (3-4 km; Barchi et al.,  
679 2021).

680 Based on the tectonic and stratigraphic similarities above exposed, we propose that  
681 the southwestern Valencia Trough may exhibit a comparable pattern of seismicity to  
682 that of central Italy. Specifically, we hypothesise that seismic events in the  
683 southwestern Valencia Trough could also have nucleated within the suprasalt  
684 succession and in the basement. Furthermore, we postulate that large earthquakes  
685 in the southwestern Valencia Trough could also rupture both mechanical layers.  
686 Available centroid data for the southwestern Valencia Trough suggest that most  
687 earthquakes nucleate at depths between 1 and 13 km (Fig. 2). Although these depth

688 estimates carry significant uncertainties, we interpret this dataset as supporting  
689 evidence for our hypothesis that seismicity in the southwestern Valencia Trough  
690 nucleates both in the basement and in the cover.

691 From this hypothesis we evaluate the seismic potential of these (unlikely) supra-salt  
692 ruptures. A widely used approach to characterise the seismic potential of an active  
693 fault involves earthquake fault scaling relationships. These relationships estimate  
694 the seismic parameters of an active fault based on its geometric and/or kinematic  
695 features (Kanamori and Anderson, 1975; Geller, 1976; Wells and Coppersmith;  
696 1994; Stirling et al., 2002 and 2013; Leonard, 2010 and 2014; among many others).  
697 In the case of the southwestern Valencia Trough faults, the available data support  
698 characterisation on the basis of geometric features, such as fault area, length, or  
699 width. However, the mechanical layering observed in the southwestern Valencia  
700 Trough necessitates the cautious application of these scaling relationships. The  
701 influence of the weak mechanical layer introduces complexities that may not be  
702 fully accounted for by traditional scaling methods.

703 As we mentioned previously, most empirical source-scaling relationships for crustal  
704 earthquakes correlate the moment magnitude ( $M_w$ ) with the fault dimensions  
705 (length, width, and/or area; Kanamori and Anderson, 1975; Geller, 1976; Wells and  
706 Coppersmith; 1994; Stirling et al., 2022; Leonard, 2010; among many others). We  
707 propose that when these scaling relationships are applied to regions with a weak  
708 mechanical layer, the role of this layer should be explicitly considered in the  
709 analysis. This is because the presence of a weak layer can potentially hinder the  
710 effective vertical propagation of a rupture, thereby limiting the effective width of the  
711 seismogenic layer. This consideration is particularly relevant for earthquakes that  
712 nucleate above the weak layer. We propose including a correction factor in the  
713 empirical relationships that explicitly accounts for cases where earthquakes are  
714 more likely to involve only part of the seismogenic layer due to mechanical  
715 heterogeneities within the crust. This factor would aim to provide a more accurate  
716 seismic characterization of faults in regions with such a structural arrangement.

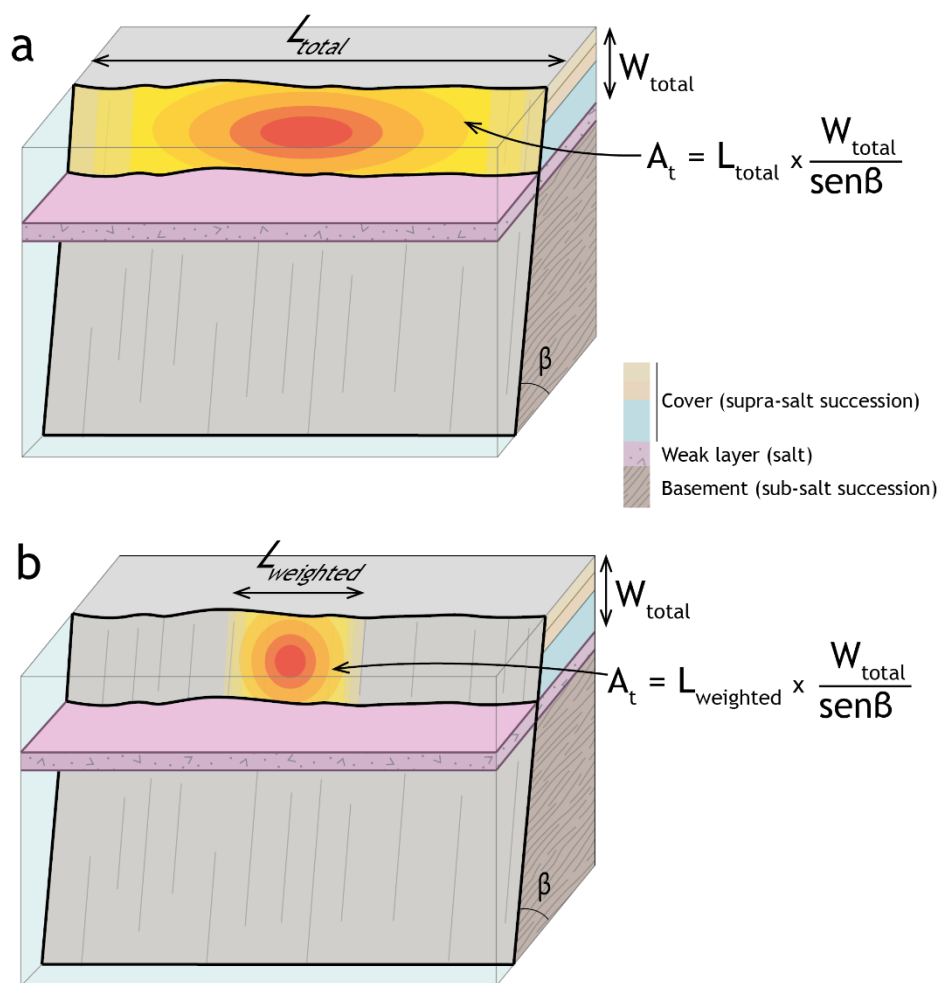
717 Several studies suggest that the downdip width of the seismogenic crust (the  
718 thickness of seismogenic crust measured along the fault plane) can constrain the

719 maximum magnitudes of earthquakes (Hyndman, 2007; Ruff and Kanamori, 1983;  
720 Weng & Yang, 2017). For large-magnitude events involving the entire seismogenic  
721 crust, some scaling relationships account for the constraint on fault-width rupture  
722 growth relative to fault-length rupture growth by incorporating a change in slope in  
723 width-to-length scaling (Leonard, 2010; Yen and Ma, 2011; Leonard, 2014; Cheng et  
724 al., 2019; Huang et al., 2024). This change in slope reflects the width of the  
725 seismogenic crust, which imposes a limit on rupture propagation owing to  
726 variations in the mechanical behaviour of the crust. We propose a similar approach  
727 to evaluate the seismic potential of regions characterised by a weak mechanical  
728 layer within the upper crust, such as the southwestern Valencia Trough.

729 Our approach involves including the rupture aspect ratio when calculating the  
730 geometric parameters of an active fault. Specifically, we propose that, instead of  
731 using the total area or length of the fault as direct inputs to scaling relationships, a  
732 correction factor should be applied to these geometric parameters. This correction  
733 factor is based on the empirical aspect ratio of faults. For example, consider an  
734 earthquake nucleating above a weak mechanical layer. Two potential scenarios for  
735 the propagation of such an earthquake can be envisioned: i) that it propagates  
736 through the basement–cover interface or ii) that it remains restricted to the  
737 succession above the weak layer. In the first scenario, the potential maximum  
738 rupture area can be calculated by multiplying the fault length by the fault width. Any  
739 area-based or length-based scaling relationship can then be applied. This scenario  
740 represents the maximum seismic potential of the fault.

741 In the second scenario, where rupture propagation is restricted to succession above  
742 the weak layer, a simplistic calculation of the fault area would multiply the total fault  
743 length by the thickness of the ruptured succession (Fig 11). However, since the  
744 hypothesised rupture offsets only the succession above the mechanically weak  
745 layer, the width of the rupture is significantly limited. This would result in a highly  
746 elongated rupture with an unusually high aspect ratio, deviating from commonly  
747 observed values (Nicol et al., 1996; Stock & Smith, 2000). For this second scenario,  
748 we propose using the thickness of the ruptured succession as a limiting factor.  
749 Specifically, the rupture area should be calculated by multiplying the width of the

750 fault (based on the thickness of the succession above the weak layer and corrected  
 751 by the fault dip) by the total fault length weighted by the aspect ratio (Fig 11). This  
 752 weighted area can then be used as input in any area-based scaling relationship. We  
 753 consider that this calculation offers a more realistic estimation of the maximum  
 754 seismogenic potential for events rupturing only the succession above the weak  
 755 layer. Finally, we recommend avoiding length-based scaling relations for this  
 756 second scenario, as such relations implicitly assume a rupture of the entire  
 757 seismogenic crust.



759 Figure 11. Conceptual model of the weighted rupture area of an earthquake  
 760 nucleating above the weak mechanical layer. The area of the rupture is  
 761 shown using a red–yellow gradient. An earthquake rupturing the total fault  
 762 length ( $L$ ) and the total thickness ( $W_{total}$ ) above the weak layer would result in  
 763 nonrealistic, highly elongated ruptures. In figure panel b, we propose a more

764 realistic case: an earthquake offsetting the total thickness above the weak  
765 layer ( $W_{\text{total}}$ ) and a rupture length weighted by the aspect ratio ( $L_w$ ).

766

767

768 **8. Seismic characterisation of active faults in the southwestern Valencia**  
769 **Trough.**

770 In this section, we compute the seismic potential of the active faults in the  
771 southwestern Valencia Trough by applying several scaling relationships. We perform  
772 two distinct calculations corresponding to the two scenarios described earlier. i) In  
773 the first scenario, we assume a rupture involving both the supra- and subsalt  
774 successions. That is, this first scenario accounts for an earthquake rupturing the  
775 entire seismogenic crust. This scenario provides the maximum seismic potential of  
776 the faults. ii) In the second scenario, we assume that a rupture is restricted to the  
777 suprasalt succession. For this calculation, we apply several area-based scaling  
778 relationships, and we use the area weighted by the aspect ratio as the input  
779 parameter. Since the rupture area involved in this second scenario is relatively  
780 small, a relatively low seismogenic potential is expected.

781

782 *8.1. First scenario: Ruptures involving the entire seismogenic crust.*

783 For both scenarios, we apply the scaling relationships of Wells & Coppersmith  
784 (1994) (values corresponding to normal faults for the Cullera and Valencia faults,  
785 and to strike slip faults for the Albufera Fault) and Stirling et al. (2002). In the first  
786 scenario, i.e., ruptures involving the entire seismogenic crust, we assume that a  
787 complete fault ruptured from the subsalt basement through the suprasalt  
788 succession. To compute the seismogenic potential of this first scenario we used the  
789 fault length and fault area as the primary input parameter (Table 1). The fault area  
790 used for these calculations was the result of multiplying the fault length by the fault  
791 width. We prefer to use this simplification instead of the areas calculated from our  
792 3D models to ensure consistency when comparing magnitude estimates derived  
793 from the methodology involving a correction factor (see below). The total thickness  
794 of the seismogenic crust in the study area is not precisely known. García-  
795 Mayordomo (2005) proposed a thickness ranging between 9 and 11 km. This value  
796 agrees with crust thicknesses based on deep seismic profiles (Etheve et al., 2016;  
797 Maillard & Mauffret, 2013; Ramos et al., 2025) as well as the lithospheric structure

798 based on P-wave receiver function analysis and seismic tomography (Mancilla et  
 799 al., 2015; Palomeras et al., 2017).. Therefore, we assumed a mean thickness of the  
 800 seismogenic crust of 10 km.

801

802 Table 1 Source parameters obtained from length- and area-based scaling  
 803 relationships (Wells & Coppersmith, 1994 -WC94- and Stirling et al., 2002 -  
 804 Stirling02-) assuming ruptures involving the entire seismogenic crust. L, fault length;  
 805  $M_w$ , moment magnitude; AD, average displacement; MD, maximum displacement.  
 806 Values computed using length-based Wells & Coppersmith (1994) relationships  
 807 refer to normal faulting (Cullera and Valencia faults) and strike-slip faulting (Albufera  
 808 Fault).

809

	Length-based relationships						Area-based relationships		
	L km	WC94			Stirling02		A km <sup>2</sup>	WC94	Stirling02
		$M_w$	AD m	MD m	$M_w$	AD m		$M_w$	$M_w$
Cullera Fault	59	7.2 ±0.34	1.61 ±0.37	4.94 ±0.41	7.3 ±0.30	2.39 ±0.24	834.4	6.91 ±0.25	7.22 ±0.26
Albufera Fault	40	6.97 ±0.34	0.99 ±0.37	2.75 ±0.41	7.16 ±0.30	2.23 ±0.24	565.7	6.74 ±0.25	7.1 ±0.26
Valencia Fault	20	6.58 ±0.34	0.42 ±0.37	0.97 ±0.41	6.92 ±0.30	1.97 ±0.24	282.9	6.43 ±0.25	6.88 ±0.26

810

811

## 812 8.2. Second scenario: Ruptures involving only the suprasalt succession

813 In this scenario, the presence of a mechanically weak layer within the seismogenic  
 814 crust is considered to control the seismic potential of active faults. As discussed  
 815 previously, we use the weighted rupture area as the input parameter for the scaling

816 relationships. The weighting factor is based on the aspect ratio of normal faults. To  
817 provide context for this approach, we also present seismic parameters calculated  
818 from the total fault area offsetting the entire suprasalt succession. The aspect ratios  
819 of normal fault ruptures vary widely (0.4–18); however, most of the observed  
820 ruptures are within the range of 0.5 to 3.5 (Nicol et al., 1996; Stock & Smith, 2000),  
821 with a mode value of 1.8 (30%, Stock & Smith, 2000). Numerical simulations of  
822 strike-slip faults by Weng & Yang (2016) demonstrated that the width of the  
823 seismogenic layer significantly influences the rupture aspect ratios. According to  
824 their findings, a seismogenic layer thickness of approximately 10 km marks a critical  
825 boundary: for thicknesses less than this value, rupture aspect ratios remain low (ca.  
826 2), whereas thicknesses greater than 10 km result in significantly higher aspect  
827 ratios (<8). Considering these findings and given that the suprasalt succession in the  
828 southwestern Valencia Trough has an average thickness of approximately 5 km, we  
829 adopt an aspect ratio of 1.8 for our calculations.

830 In the southwestern Valencia Trough, the suprasalt succession thickness at the  
831 location of active faults varies. We used thicknesses of 5 km, 3.3 km and 2.3 km for  
832 the Cullera, Valencia, and Albufera faults respectively, as input values for our  
833 calculation. For events unrestricted by the aspect ratio (i.e., earthquakes rupturing  
834 the entire fault length and width of the suprasalt succession), we compute the  
835 rupture area as the product of length and width accounting also for the fault dip  
836 ( $L \cdot W / \sin \beta$ ). However, when the seismic potential for ruptures weighted by the  
837 aspect ratio is calculated, the controlling factor is the fault width.

838

839 Table 2 Moment magnitude obtained from scaling relationships (Wells &  
840 Coppersmith, 1994 -WC94- and Stirling et al., 2002 -Stirling02-). The first column  
841 (not weighted area) corresponds to the values obtained assuming ruptures involving  
842 the total suprasalt succession. The second column (weighted area) shows the  
843 values obtained using the area weighted by the aspect ratio as input parameter.

844

	Not weighted area			Weighted area		
	Input parameters A km <sup>2</sup>	M <sub>w</sub> WC94	M <sub>w</sub> Stirling02	Input parameters A km <sup>2</sup>	M <sub>w</sub> WC94	M <sub>w</sub> Stirling02
Cullera Fault	360	6.54 ±0.34	6.96 ±0.26	67	5.79 ±0.34	6.42 ±0.26
Albufera Fault	112	6.02 ±0.34	6.59 ±0.26	14	5.16 ±0.34	5.93 ±0.26
Valencia Fault	81	5.87 ±0.34	6.48 ±0.26	29	5.42 ±0.34	6.16 ±0.26

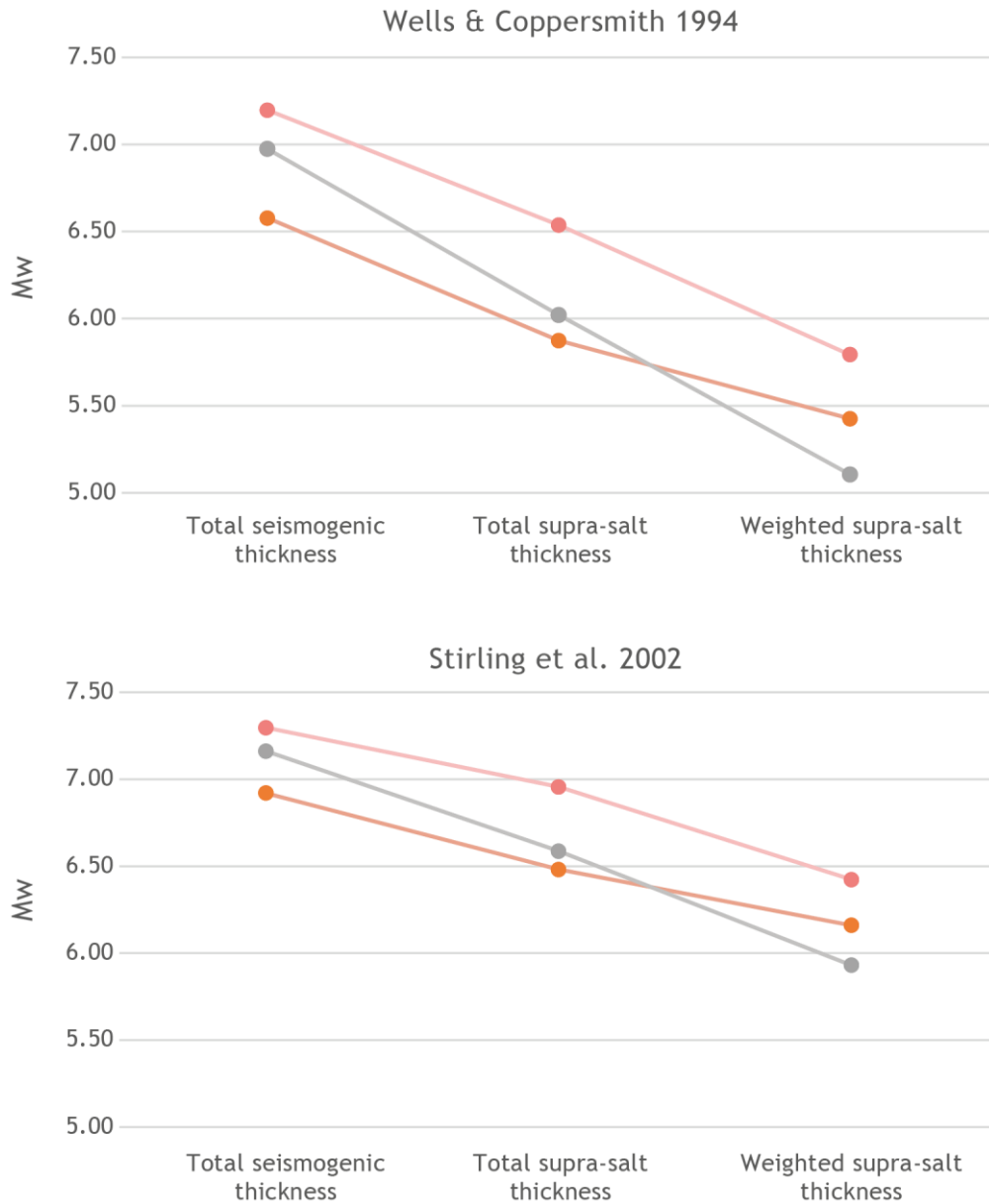
845

846 The comparison between the standard application of earthquake source scaling  
847 relations and the approach presented here for regions characterised by the  
848 presence of a weak mechanical layer within the seismogenic crust reveals  
849 significant differences (Fig. 12). The maximum expected magnitudes for  
850 characteristic events rupturing the entire seismogenic crust (i.e., propagating  
851 across the basement–cover interface) are estimated to be 6.9–7.3, 6.4–6.9, and 6.7–  
852 7.2 for the Cullera, Valencia, and Albufera Faults, respectively. In contrast, for  
853 hypothetical earthquakes restricted to the suprasalt succession and rupturing of  
854 the total length of the faults, the expected magnitudes are lower, ranging from 6.54–  
855 6.96, 5.87–6.48, 6.02–6.59 for the Cullera, Valencia, and Albufera faults,  
856 respectively. However, in such cases, we argue that the seismic potential derived  
857 using area-weighted relations provides a more realistic estimate. Using this  
858 approach, our calculations yield maximum magnitudes of 5.79–6.42, 5.42–6.16, and  
859 5.11–5.93 for the Cullera, Valencia, and Albufera faults, respectively. These values  
860 are 5–15 % lower than those obtained when accounting for the total suprasalt  
861 succession thickness.

862 When the area-weighted values are compared with the maximum expected  
863 magnitudes for ruptures involving the entire seismogenic crust, the results reveal a  
864 11–26% reduction. This discrepancy highlights the importance of incorporating  
865 mechanical layering into seismic potential assessments in regions where weak

866 layers influence fault dynamics and rupture propagation. Furthermore, these  
867 differences in seismic potential should be addressed in probabilistic seismic hazard  
868 assessments.

869



870

871 Figure 12. Plots of  $M_w$  values for the Cullera, Albufera and Valencia Faults obtained  
872 using the scaling relationships of Wells & Coppersmith (1994) and Stirling et al.  
873 (2002). The plots show the values computed assuming a rupture of the total  
874 seismogenic thickness, a rupture of the total suprasalt succession, and the values  
875 assuming a rupture of an area calculated using a suprasalt thickness weighted with  
876 the aspect ratio.



## 878 **9. Conclusions**

879 Analysis of a comprehensive subsurface dataset from the southwestern Valencia  
880 Trough enables the identification of three major active faults: the normal Cullera  
881 Fault, the oblique Albufera Fault, and the normal Valencia Fault. Among these  
882 faults, the Cullera Fault is the main active structure in this region, with a cumulative  
883 offset of 1800 m at the top of the Messinian marker. The long-term slip rate varies  
884 over time between  $0.15 \pm 0.1$  mm/y and  $0.4 \pm 0.1$  mm/y. The Albufera Fault, which is  
885 55 km in length, has a long-term slip rate of  $0.2 \pm 0.1$  mm/y, whereas the 20-km-long  
886 Valencia Fault significantly influences the spatial distribution of Quaternary  
887 depocentres.

888 Our results also reveal a 10-km-thick heterogeneous seismogenic crust in the study  
889 area, largely because of a mechanically weak layer, which is composed mainly of  
890 Triassic evaporites. Consequently, two competing mechanisms are responsible for  
891 the offset along the active faults: tectonics and salt withdrawal. A quantitative  
892 evolutionary analysis of the Cullera Fault indicates that tectonics was the dominant  
893 mechanism during the Pliocene, whereas salt withdrawal took precedence in the  
894 early Quaternary (2.6–2 Ma). After 2 Ma, tectonic activity once again became the  
895 primary driver of fault displacement.

896 Using standard scaling relationships, we computed maximum expected  
897 magnitudes for the southwestern Valencia Trough faults. These maximum expected  
898 magnitudes range between 6.9–7.3 for the Cullera Fault, 6.7–7.2 for the Albufera  
899 Fault, and 6.4–6.9 for de Valencia Fault. However, the mechanically layered crust of  
900 the southwestern Valencia Trough influences seismicity: events may nucleate in  
901 either the basement or the suprasalt succession. Moreover, the weak layer could  
902 influence the vertical propagation of a potential rupture. That is, total or partial  
903 decoupling related to the mechanically weak layer implies that an earthquake that  
904 nucleated in the suprasalt succession would likely be restricted to this upper part of  
905 the seismogenic crust, yet larger events involving basement and cover units are also  
906 plausible. For reliable seismic hazard assessments, both scenarios must be  
907 accounted for. To compute the seismogenic potential of active faults under the  
908 assumption of rupture within the suprasalt succession, we propose the use of the

909 rupture aspect ratio as a correction factor for the maximum rupture area.  
910 Specifically, the product of the suprasalt thickness (corrected by the fault dip) and  
911 the fault length—weighted by the aspect ratio—provides a more realistic  
912 approximation of the maximum rupture area. Using this method, the maximum  
913 magnitudes for suprasalt ruptures of the southwestern Valencia Trough faults are  
914 5.79-6.42, 5.42-6.16, and 5.11-5.93 for the Cullera, Valencia, and Albufera faults,  
915 respectively. These values are 5-15% lower than those obtained by considering the  
916 full suprasalt thickness alone, and 11-26% lower than estimates involving the entire  
917 seismogenic crust.

918 Overall, these findings greatly enhance our understanding of the seismogenic  
919 potential of the southwestern Valencia Trough, an offshore area near densely  
920 populated areas. These findings provide a basis for improved seismic hazard  
921 assessments. Additionally, as we are addressing offshore faults exhibiting vertical  
922 displacement, our findings can be used to establish the tsunamigenic potential of  
923 this region. Furthermore, this approach for incorporating mechanical  
924 heterogeneities in the seismogenic crust can be applied to other regions and  
925 tectonic settings with analogous structural configurations.

926

927

928 **10. Author contribution**

929 Martin-Rojas, I.: Conceptualization, Data curation, Formal analysis, Funding  
930 acquisition, Investigation, Methodology, Project administration, Supervision,  
931 Validation, Visualization, Writing – original draft preparation, review & editing

932 Ramos, A.; Data curation, Formal analysis, Funding acquisition, Investigation,  
933 Resources, Visualization, Writing – original draft preparation, review & editing

934 De Ruig, M.: Data curation, Formal analysis, Investigation, Resources,  
935 Visualization, Writing – original draft preparation, review & editing

936 Medina-Cascales, I.: Data curation, Formal analysis, Investigation, Visualization,  
937 Writing – review & editing

938 Santamaría-Pérez, E.: Data curation, Formal analysis, Investigation, Writing –  
939 review & editing

940 Alfaro, P.: Data curation, Formal analysis, Investigation, Supervision, Writing –  
941 review & editing

942

943 **11. Competing interests**

944 The authors declare that they have no conflict of interest.

945

946 **12. Acknowledgements**

947 We acknowledge the comments of the Raúl Pérez-López, an anonymous reviewer,  
948 and the Editor [Solmaz Mohadjer](#), which significantly improved the quality of this  
949 paper.

950

951 **13. Financial support**

952 This research was funded by the Spanish Ministry of Science, Innovation and  
953 University (research projects PID2021-127967NB-I00 and RTI2018-100737-B-I00),  
954 Generalitat Valenciana (Valencian Regional Government, research projects  
955 AICO2021/196 and CIAPOS/2022/082, and University of Alicante (research project  
956 VIGROB053). The authors acknowledge the use of the MOVE Software Suite granted  
957 by PE Limited (Petex).

958 **14. References**

- 959 Agustí, J., Santos-Cubedo, A., Furió, M., De Marfá, R., Blain, H., Oms, O., & Sevilla, P.  
960 (2011). The late Neogene-early Quaternary small vertebrate succession from the  
961 Almenara-Casablanca karst complex (Castellón, Eastern Spain): Chronologic and  
962 paleoclimatic context. *Quaternary International*, 243(1), 183–191.  
963 10.1016/j.quaint.2010.11.016
- 964 Albarracín, S., Alcántara-Carrió, J., Barranco, A., Sánchez García, M. J., Fontán Bouzas, Á,  
965 & Rey Salgado, J. (2013). Seismic evidence for the preservation of several stacked  
966 Pleistocene coastal barrier/lagoon systems on the Gulf of Valencia continental shelf  
967 (western Mediterranean). *Geo-Marine Letters*, 33(2-3), 217–223. 10.1007/s00367-  
968 012-0315-x
- 969 Arche, A., & López-Gómez, J. (1996). Origin of the Permian-Triassic Iberian Basin, central-  
970 eastern Spain. *Tectonophysics*, 266(1), 443–464. 10.1016/S0040-1951(96)00202-8
- 971 Barchi, M. R., Carboni, F., Michele, M., Ercoli, M., Giorgetti, C., Porreca, M., Azzaro, S., &  
972 Chiaraluce, L. (2021). The influence of subsurface geology on the distribution of  
973 earthquakes during the 2016–2017 Central Italy seismic sequence. *Tectonophysics*,  
974 807, 228797. <https://doi.org/10.1016/j.tecto.2021.228797>
- 975 Barchi, M. R., & Mirabella, F. (2009). The 1997–98 Umbria–Marche earthquake sequence:  
976 “Geological” vs. “seismological” faults. *Tectonophysics*, 476(1–2), 170–179.  
977 <https://doi.org/10.1016/j.tecto.2008.09.013>
- 978 Boncio, P., Lavecchia, G., & Pace, B. (2004). Defining a model of 3D seismogenic sources  
979 for Seismic Hazard Assessment applications: The case of central Apennines (Italy).

980 Journal of Seismology, 8(3), 407–425.  
981 <https://doi.org/10.1023/B:JOSE.0000038449.78801.05>

982 Buforn, E., & Udías, A. (2021). *El terremoto de Alcoy de 1620 y la serie sísmica de 1644 en*  
983 *la comarca de Muro*. Centro Nacional de Información Geográfica.

984 Buforn, E., Udías, A., Sanz de Galdeano, C., & Cesca, S. (2015). The 1748 Montesa  
985 (southeast Spain) earthquake — A singular event. *Tectonophysics*, 664, 139–153.  
986 10.1016/j.tecto.2015.09.005

987 Cameselle, A. L., Urgeles, R., De Mol, B., Camerlenghi, A., & Canning, J. C. (2014). Late  
988 Miocene sedimentary architecture of the Ebro Continental Margin (Western  
989 Mediterranean): implications to the Messinian Salinity Crisis. *International Journal of*  
990 *Earth Sciences : Geologische Rundschau*, 103(2), 423–440. 10.1007/s00531-013-  
991 0966-5

992 Casciello, E., Vergés, J., Saura, E., Casini, G., Fernández, N., Blanc, E., Homke, S., & Hunt,  
993 D. W. (2009). Fold patterns and multilayer rheology of the Lurestan Province, Zagros  
994 simply folded belt (Iran). *Journal of the Geological Society*, 166(5), 947–959.  
995 10.1144/0016-76492008-138

996 Cheng Jia, C. J., Rong, Y., Magistrale, H., Chen Guihua, C. G., & Xu Xiwei, X. X. (2019a).  
997 Earthquake rupture scaling relations for mainland China. *Seismological Research*  
998 *Letters*, 91(1), 248–261. 10.1785/0220190129

999 Cheng Jia, C. J., Rong, Y., Magistrale, H., Chen Guihua, C. G., & Xu Xiwei, X. X. (2019b).  
1000 Earthquake rupture scaling relations for mainland China. *Seismological Research*  
1001 *Letters*, 91(1), 248–261. 10.1785/0220190129

1002 Chiaraluce, L., Di Stefano, R., Tinti, E., Scognamiglio, L., Michele, M., Casarotti, E.,  
1003 Cattaneo, M., De Gori, P., Chiarabba, C., Monachesi, G., Lombardi, A., Valoroso, L.,  
1004 Latorre, D., & Marzorati, S. (2017). The 2016 Central Italy Seismic Sequence: A First  
1005 Look at the Mainshocks, Aftershocks, and Source Models. *Seismological Research*  
1006 *Letters*, 88(3), 757–771. <https://doi.org/10.1785/0220160221>

1007 Chiaraluce, L., Ellsworth, W. L., Chiarabba, C., & Cocco, M. (2003). Imaging the  
1008 complexity of an active normal fault system: The 1997 Colfiorito (central Italy) case  
1009 study. *Journal of Geophysical Research: Solid Earth*, 108(B6).  
1010 <https://doi.org/10.1029/2002JB002166>

1011 Clavell, E., & Berastegui, X. (1991). Petroleum geology of the Gulf of Valencia. *Generation,*  
1012 *Accumulation, and Production of Europe's Hydrocarbons*, , 355–368.  
1013 [https://www.scopus.com/inward/record.uri?eid=2-s2.0-](https://www.scopus.com/inward/record.uri?eid=2-s2.0-0026310072&partnerID=40&md5=8f34c3d495738519a9101eb775a91bd4)  
1014 [0026310072&partnerID=40&md5=8f34c3d495738519a9101eb775a91bd4](https://www.scopus.com/inward/record.uri?eid=2-s2.0-0026310072&partnerID=40&md5=8f34c3d495738519a9101eb775a91bd4)

1015 De Ruig, & M.J. (1992). *Tectono-sedimentary evolution of the Prebetic fold belt of Alicante*

1016 Del Rio, V. D., Rey, J., & Vegas, R. (1986). The Gulf of Valencia continental shelf:  
1017 Extensional tectonics in Neogene and Quaternary sediments. *Marine Geology*, 73(1),  
1018 169–179. 10.1016/0025-3227(86)90117-9

1019 DeMets, C., Gordon, R. G., Argus, D. F., & Stein, S. (1994). Effect of recent revisions to the  
1020 geomagnetic reversal time scale on estimates of current plate motions. *Geophysical*  
1021 *Research Letters*, 21(20), 2191–2194. 10.1029/94GL02118

1022 Duffy, O. B., Gawthorpe, R. L., & Docherty, M. (2023). Tectono-stratigraphic evolution of  
1023 salt-influenced normal fault systems: an example from the Coffee-Soil Fault, Danish  
1024 North Sea. *Journal of the Geological Society*, 180(6), 1. 10.1144/jgs2023-016

- 1025 Etheve, N., Frizon de Lamotte, D., Mohn, G., Martos, R., Roca, E., & Blanpied, C. (2016).  
1026 Extensional vs contractional Cenozoic deformation in Ibiza (Balearic Promontory,  
1027 Spain): Integration in the West Mediterranean back-arc setting. *Tectonophysics*, 682,  
1028 35–55. 10.1016/j.tecto.2016.05.037
- 1029 Faccenna, C., Piromallo, C., Crespo-Blanc, A., Jolivet, L., & Rossetti, F. (2004a). Lateral  
1030 slab deformation and the origin of the western Mediterranean arcs. *Tectonics*  
1031 (*Washington, D.C.*), 23(1), np–n/a. 10.1029/2002TC001488
- 1032 Faccenna, C., Piromallo, C., Crespo-Blanc, A., Jolivet, L., & Rossetti, F. (2004b). Lateral  
1033 slab deformation and the origin of the western Mediterranean arcs. *Tectonics*  
1034 (*Washington, D.C.*), 23(1), np–n/a. 10.1029/2002TC001488
- 1035 Fang, P., Tugend, J., Mohn, G., Kusznir, N., & Ding, W. (2021a). Evidence for rapid large-  
1036 amplitude vertical motions in the Valencia Trough (Western Mediterranean)  
1037 generated by 3D subduction slab roll-back. *Earth and Planetary Science Letters*, 575,  
1038 117179. 10.1016/j.epsl.2021.117179
- 1039 Fang, P., Tugend, J., Mohn, G., Kusznir, N., & Ding, W. (2021b). Evidence for rapid large-  
1040 amplitude vertical motions in the Valencia Trough (Western Mediterranean)  
1041 generated by 3D subduction slab roll-back. *Earth and Planetary Science Letters*, 575,  
1042 117179. 10.1016/j.epsl.2021.117179
- 1043 Ford, M., Le Carlier de Veslud, C., & Bourgeois, O. (2007). Kinematic and geometric  
1044 analysis of fault-related folds in a rift setting: The Dannemarie basin, Upper Rhine  
1045 Graben, France. *Journal of Structural Geology*, 29(11), 1811–1830.  
1046 10.1016/j.jsg.2007.08.001

- 1047 García-Mayordomo, J., Insua-Arévalo, J. M., Martínez-Díaz, J. J., Jiménez-Díaz, A., Martín-  
1048 Banda, R., Martín-Alfageme, S., Álvarez-Gómez, J. A., Rodríguez-Peces, M., Pérez-  
1049 López, R., Rodríguez-Pascua, M. A., Masana, E., Perea, H., Martín-González, F.,  
1050 Giner-Robles, J., Nemser, E. S., & Cabral, J. (2012). The Quaternary active faults  
1051 database of Iberia (QAFI v. 2.0). *Journal of Iberian Geology*,  
1052 38(1)10.5209/rev\_JIGE.2012.v38.n1.39219
- 1053 Gaspar-Escribano, J. M., Garcia-Castellanos, D., Roca, E., & Cloetingh, S. (2004).  
1054 Cenozoic vertical motions of the Catalan Coastal Ranges (NE Spain): The role of  
1055 tectonics, isostasy, and surface transport. *Tectonics (Washington, D.C.)*, 23(1), np–  
1056 n/a. 10.1029/2003TC001511
- 1057 Geel, T. (1995). Oligocene to early Miocene tectono-sedimentary history of the Alicante  
1058 region (SE Spain): implications for Western Mediterranean evolution. *Basin Research*,  
1059 7(4), 313–336. 10.1111/j.1365-2117.1995.tb00120.x
- 1060 Geller, R. J. (1976). Scaling relations for earthquake source parameters and magnitudes.  
1061 *Bulletin of the Seismological Society of America*, 66(5), 1501–1523.  
1062 <https://pubs.geoscienceworld.org/ssa/bssa/article/66/5/1501/117604>
- 1063 González, Á. (2017). The Spanish National Earthquake Catalogue: Evolution, precision and  
1064 completeness. *Journal of Seismology*, 21(3), 435–471. 10.1007/s10950-016-9610-8
- 1065 Guimera, J., & Alvaro, M. (1990). Structure et évolution de la compression alpine dans la  
1066 Chaîne ibérique et la Chaîne côtière catalane (Espagne). *Bulletin De La Société*  
1067 *Géologique De France*, 6(2), 339–348. 10.2113/gssgfbull.VI.2.339

1068 Hongxing, G., & Anderson, J. K. (2007). Fault throw profile and kinematics of Normal fault:  
1069 conceptual models and geologic examples. *Geological Journal of China Universities*,  
1070 13(1), 75.

1071 Huang, J., Abrahamson, N. A., Sung, C., & Chao, S. (2024). New Empirical Source-Scaling  
1072 Laws for Crustal Earthquakes Incorporating Fault Dip and Seismogenic-Thickness  
1073 Effects. *Seismological Research Letters*, 95(4), 2352–2367. 10.1785/0220240034

1074 Hyndman, R. D., Yamano, M., & Oleskevich, D. A. (1997). The seismogenic zone of  
1075 subduction thrust faults. *Island Arc*, 6(3), 244–260. 10.1111/j.1440-  
1076 1738.1997.tb00175.x

1077 Improta, L., Latorre, D., Margheriti, L., Nardi, A., Marchetti, A., Lombardi, A. M., Castello,  
1078 B., Villani, F., Ciaccio, M. G., Mele, F. M., Moretti, M., Battelli, P., Berardi, M.,  
1079 Castellano, C., Melorio, C., Modica, G., Pirro, M., Rossi, A., Thermes, C., ... Di Maro,  
1080 R. (2019). Multi-segment rupture of the 2016 Amatrice-Visso-Norcia seismic  
1081 sequence (central Italy) constrained by the first high-quality catalog of Early  
1082 Aftershocks. *Scientific Reports*, 9(1), 6921. [https://doi.org/10.1038/s41598-019-](https://doi.org/10.1038/s41598-019-43393-2)  
1083 [43393-2](https://doi.org/10.1038/s41598-019-43393-2)

1084 IGN. (2025). *Instituto Geográfico Nacional (2025) Servicio de Información Sísmica*.

1085 Jackson, C. A. -, & Rotevatn, A. (2013). 3D seismic analysis of the structure and evolution  
1086 of a salt-influenced normal fault zone: A test of competing fault growth models.  
1087 *Journal of Structural Geology*, 54, 215–234. 10.1016/j.jsg.2013.06.012

1088 Jackson, M. P. A., & Hudec, M. R. (2005). Stratigraphic record of translation down ramps in  
1089 a passive-margin salt detachment. *Journal of Structural Geology*, 27(5), 889–911.  
1090 10.1016/j.jsg.2005.01.010

- 1091 Jolivet, L., & Faccenna, C. (2000). Mediterranean extension and the Africa-Eurasia  
1092 collision. *Tectonics*, 19(6), 1095–1106. 10.1029/2000TC900018
- 1093 Kanamori, H., & Anderson, D. L. (1975). Theoretical basis of some empirical relations in  
1094 seismology. *Bulletin of the Seismological Society of America*, 65(5), 1073–1095.  
1095 <https://pubs.geoscienceworld.org/ssa/bssa/article/65/5/1073/117458>
- 1096 Kane, K. E., Jackson, C. A. -, & Larsen, E. (2010). Normal fault growth and fault-related  
1097 folding in a salt-influenced rift basin: South Viking Graben, offshore Norway. *Journal*  
1098 *of Structural Geology*, 32(4), 490–506. 10.1016/j.jsg.2010.02.005
- 1099 Leonard, M. (2010). Earthquake fault scaling; self-consistent relating of rupture length,  
1100 width, average displacement, and moment release. *Bulletin of the Seismological*  
1101 *Society of America*, 100(5A), 1971–1988. 10.1785/0120090189
- 1102 Leonard, M. (2014). Self-consistent earthquake fault-scaling relations; update and  
1103 extension to stable continental strike-slip faults. *Bulletin of the Seismological Society*  
1104 *of America*, 104(6), 2953–2965. 10.1785/0120140087
- 1105 Lirer, F., Foresi, L. M., Iaccarino, S. M., Salvatorini, G., Turco, E., Cosentino, C., Sierro, F.  
1106 J., & Caruso, A. (2019). Mediterranean Neogene planktonic foraminifer biozonation  
1107 and biochronology. *Earth-Science Reviews*, 196, 102869.  
1108 10.1016/j.earscirev.2019.05.013
- 1109 Lofi, J. (2011). *Seismic atlas of the "Messinian salinity crisis" markers in the Mediterranean*  
1110 *and Black Seas*. Commission for the Geological Map of the World.

- 1111 Maillard, A., Mauffret, A., Watts, A. B., Torné, M., Pascal, G., Buhl, P., & Pinet, B. (1992).  
1112 Tertiary sedimentary history and structure of the Valencia trough (western  
1113 Mediterranean). *Tectonophysics*, 203(1), 57–75. 10.1016/0040-1951(92)90215-R
- 1114 Maillard, A., & Mauffret, A. (2013). Structure and present-day compression in the offshore  
1115 area between Alicante and Ibiza Island (Eastern Iberian Margin). *Tectonophysics*,  
1116 591, 116–130. 10.1016/j.tecto.2011.07.007
- 1117 Mansfield, C. S., & Cartwright, J. A. (1996). High resolution fault displacement mapping  
1118 from three-dimensional seismic data: evidence for dip linkage during fault growth.  
1119 *Journal of Structural Geology*, 18(2), 249–263. 10.1016/S0191-8141(96)80048-4
- 1120 Marsh, N., Imber, J., Holdsworth, R. E., Brockbank, P., & Ringrose, P. (2010). The structural  
1121 evolution of the Halten Terrace, offshore Mid-Norway: extensional fault growth and  
1122 strain localisation in a multi-layer brittle-ductile system. *Basin Research*, 22(2), 195–  
1123 214. 10.1111/j.1365-2117.2009.00404.x
- 1124 Martí, J., Mitjavila, J., Roca, E., & Aparicio, A. (1992). Cenozoic magmatism of the valencia  
1125 trough (western mediterranean): Relationship between structural evolution and  
1126 volcanism. *Tectonophysics*, 203(1), 145–165. 10.1016/0040-1951(92)90221-Q
- 1127 Martínez-Solares, J. M., & Mezcuca, J. (2002). *Catálogo sísmico de la Península Ibérica*.  
1128 Madrid (Spain): Instituto Geográfico Nacional.
- 1129 Martinis, B., & Pieri, M. (1969). Alcune informazioni sulla formazione evaporitica del  
1130 Triassico superiore nell'Italia centrale meridionale. *Memorie Della Società Geologica  
1131 Italiana*, 4, 649–678.

- 1132 Maurin, J., & Niviere, B. (1999). Extensional forced folding and décollement of the pre-rift  
1133 series along the Rhine graben and their influence on the geometry of the syn-rift  
1134 sequences. *Forced Folds and Fractures* (pp. 73–86). The Geological Society of  
1135 London. 10.1144/GSL.SP.2000.169.01.06
- 1136 McClusky, S., Reilinger, R., Mahmoud, S., Ben Sari, D., & Tealeb, A. (2003). GPS  
1137 constraints on Africa (Nubia) and Arabia plate motions. *Geophysical Journal  
1138 International*, 155(1), 126–138. 10.1046/j.1365-246X.2003.02023.x
- 1139 Michele, M., Chiaraluce, L., Di Stefano, R., & Waldhauser, F. (2020). Fine-Scale Structure  
1140 of the 2016–2017 Central Italy Seismic Sequence From Data Recorded at the Italian  
1141 National Network. *Journal of Geophysical Research: Solid Earth*, 125(4).  
1142 <https://doi.org/10.1029/2019JB018440>
- 1143 Molinaro, M., Leturmy, P., Guezou, J. -, Frizon de Lamotte, D., & Eshraghi, S. A. (2005).  
1144 The structure and kinematics of the southeastern Zagros fold-thrust belt, Iran: From  
1145 thin-skinned to thick-skinned tectonics. *Tectonics*, 24(3), np–n/a.  
1146 10.1029/2004TC001633
- 1147 Morley, C. K., Back, S., Van Rensbergen, P., Crevello, P., & Lambiase, J. J. (2003).  
1148 Characteristics of repeated, detached, Miocene–Pliocene tectonic inversion events,  
1149 in a large delta province on an active margin, Brunei Darussalam, Borneo. *Journal of  
1150 Structural Geology*, 25(7), 1147–1169. 10.1016/S0191-8141(02)00130-X
- 1151 NEBOT, M., & GUIMERÀ, J. (2018). Kinematic evolution of a fold-and-thrust belt developed  
1152 during basin inversion: the Mesozoic Maestrat basin, E Iberian Chain. *Geological  
1153 Magazine*, 155(3), 630–640. 10.1017/S001675681600090X

- 1154 Nicol, A., Watterson, J., Walsh, J. J., & Childs, C. (1996). The shapes, major axis  
1155 orientations and displacement patterns of fault surfaces. *Journal of Structural*  
1156 *Geology*, 18(2), 235–248. 10.1016/S0191-8141(96)80047-2
- 1157 Nissen, E., Ghorashi, M., Jackson, J., Parsons, B., & Talebian, M. (2007). The 2005 Qeshm  
1158 Island earthquake (Iran)—a link between buried reverse faulting and surface folding  
1159 in the Zagros Simply Folded Belt? *Geophysical Journal International*, 171(1), 326–338.  
1160 10.1111/j.1365-246X.2007.03514.x
- 1161 Nissen, E., Tatar, M., Jackson, J. A., & Allen, M. B. (2011). New views on earthquake  
1162 faulting in the Zagros fold-and-thrust belt of Iran. *Geophysical Journal International*,  
1163 186(3), 928–944. 10.1111/j.1365-246X.2011.05119.x
- 1164 Nocquet, J. -, & Calais, E. (2003). Crustal velocity field of western Europe from permanent  
1165 GPS array solutions, 1996–2001. *Geophysical Journal International*, 154(1), 72–88.  
1166 10.1046/j.1365-246X.2003.01935.x
- 1167 Nocquet, J. (2012). Present-day kinematics of the Mediterranean: A comprehensive  
1168 overview of GPS results. *Tectonophysics*, 579, 220–242. 10.1016/j.tecto.2012.03.037
- 1169 Palano, M., González, P. J., & Fernández, J. (2015). The Diffuse Plate boundary of Nubia  
1170 and Iberia in the Western Mediterranean: Crustal deformation evidence for viscous  
1171 coupling and fragmented lithosphere. *Earth and Planetary Science Letters*, 430, 439–  
1172 447. 10.1016/j.epsl.2015.08.040
- 1173 Pascal, G., Torné, M., Buhl, P., Watts, A. B., & Mauffret, A. (1992). Crustal and velocity  
1174 structure of the Valencia trough (western Mediterranean), Part II. Detailed  
1175 interpretation of five Expanded Spread Profiles. *Tectonophysics*, 203(1), 21–35.  
1176 10.1016/0040-1951(92)90213-P

- 1177 Pascoe, R., Hooper, R., Storhaug, K., & Harper, H. (Jan 1, 1999). Evolution of extensional  
1178 styles at the southern termination of the Nordland Ridge, Mid-Norway: a response to  
1179 variations in coupling above Triassic salt. Paper presented at the , 5(1) 83–90.  
1180 10.1144/0050083 <https://www.lyellcollection.org/doi/10.1144/0050083>
- 1181 Perea, H. (2006). *Falles actives i perillositat sísmica al marge nord-occidental del solc de*  
1182 *València*
- 1183 Pérez-Peña, A., Martín-Davila, J., Gárate, J., Berrocoso, M., & Buforn, E. (2010). Velocity  
1184 field and tectonic strain in Southern Spain and surrounding areas derived from GPS  
1185 episodic measurements. *Journal of Geodynamics*, 49(3), 232–240.  
1186 10.1016/j.jog.2010.01.015
- 1187 Ramos, A., Lopez-Mir, B., Wilson, E. P., Granado, P., & Muñoz, J. A. (2020). 3D  
1188 reconstruction of syn-tectonic strata in a salt-related orogen: learnings from the Lleret  
1189 syncline (South-central Pyrenees). *Acta Geologica Hispanica*, 18(1), 1–19.  
1190 10.1344/GeologicaActa2020.18.20
- 1191 Ramos, A., de Ruig, M. J., Pedrera, A., Alfaro, P., & Martin-Rojas, I. (2025). Salt expulsion  
1192 triggered by prograding clinoforms in the SW Valencia Trough (SE Spain). *Marine and*  
1193 *Petroleum Geology*, 173, 107268. 10.1016/j.marpetgeo.2024.107268
- 1194 Ramos, A., Pedrera, A., García-Senz, J., López-Mir, B., & Salas, R. (2023). Seismic  
1195 evidence for ductile necking of the mid-lower crust beneath the Columbrets Basin  
1196 (Western Mediterranean). *Terra Nova (Oxford, England)*, 35(5), 404–412.  
1197 10.1111/ter.12664
- 1198 Rehault, J., Boillot, G., & Mauffret, A. (1984). The Western Mediterranean Basin geological  
1199 evolution. *Marine Geology*, 55(3), 447–477. 10.1016/0025-3227(84)90081-1

- 1200 Ribó, M., Puig, P., Muñoz, A., Lo Iacono, C., Masqué, P., Palanques, A., Acosta, J., Guillén,  
1201 J., & Gómez Ballesteros, M. (2016a). Morphobathymetric analysis of the large fine-  
1202 grained sediment waves over the Gulf of Valencia continental slope (NW  
1203 Mediterranean). *Geomorphology*, 253, 22–37. 10.1016/j.geomorph.2015.09.027
- 1204 Ribó, M., Puig, P., Urgeles, R., Van Rooij, D., & Muñoz, A. (2016b). Spatio-temporal  
1205 evolution of sediment waves developed on the Gulf of Valencia margin (NW  
1206 Mediterranean) during the Plio-Quaternary. *Marine Geology*, 378, 276–291.  
1207 10.1016/j.margeo.2015.11.011
- 1208 Richardson, N. J., Underhill, J. R., & Lewis, G. (2005). The role of evaporite mobility in  
1209 modifying subsidence patterns during normal fault growth and linkage, Halten  
1210 Terrace, Mid-Norway. *Basin Research*, 17(2), 203–223. 10.1111/j.1365-  
1211 2117.2005.00250.x
- 1212 Roca, E. (1994). La evolución geodinámica de la Cuenca Catalano-Balear y áreas  
1213 adyacentes desde el Mesozoico hasta la actualidad. *Acta Geologica Hispanica*,  
1214 29(1), 3–25. <https://raco.cat/index.php/ActaGeologica/article/view/75462>
- 1215 Roca, E. (2001). The Northwest Mediterranean Basin (Valencia Trough, Gulf of Lions and  
1216 Liguro-Provencal basins): structure and geodynamic evolution. *Mem. Mus. Natl. Hist.*  
1217 *Nat. (France)* (pp. 671–706)
- 1218 Roca, E., Frizon de Lamotte, D., Mauffret, A., Bracene, R., Verges, J., Benaouali, N.,  
1219 Fernandez, M., Muñoz, J. A., & Zeyen, H. (2004). TRANSMED-transect II (Aquitaine  
1220 basin, Pyrenees, Ebro basin, Catalan coastal ranges, Valencia trough, Balearic  
1221 promontory, Algerian basin, Tell, Sahara Atlas, Sahara platform). In : W. Cavazza, F.  
1222 Roure, W. Spakman, G.M. Stampfli and P.A. Ziegler (Eds). The TRANSMED Atlas - the

- 1223 Mediterranean region from Crust to Mantle. *Springer, Berlin* <https://hal.science/hal->
- 1224 [00069583](https://hal.science/hal-00069583)
- 1225 Roca, E., & Desegaulx, P. (1992). Analysis of the geological evolution and vertical
- 1226 movements in the València Trough area, western Mediterranean. *Marine and*
- 1227 *Petroleum Geology*, 9(2), 167,IN1,177–176,IN8,185. 10.1016/0264-8172(92)90089-W
- 1228 Roca, E., & Guimerà, J. (1992). The Neogene structure of the eastern Iberian margin:
- 1229 Structural constraints on the crustal evolution of the Valencia trough (western
- 1230 Mediterranean). *Tectonophysics*, 203(1), 203–218. 10.1016/0040-1951(92)90224-T
- 1231 Roca, E., Sans, M., Cabrera, L., & Marzo, M. (1999). Oligocene to Middle Miocene
- 1232 evolution of the central Catalan margin (northwestern Mediterranean).
- 1233 *Tectonophysics*, 315(1), 209–229. 10.1016/S0040-1951(99)00289-9
- 1234 Rouby, D., Guillocheau, F., Robin, C., Bouroullec, R., Raillard, S., Castelltort, S., & Nalpas,
- 1235 T. (2003). Rates of deformation of an extensional growth fault/raft system (offshore
- 1236 Congo, West African margin) from combined accommodation measurements and 3-
- 1237 D restoration. *Basin Research*, 15(2), 183–200. 10.1046/j.1365-2117.2003.00200.x
- 1238 Roustaei, M., Nissen, E., Abbassi, M., Gholamzadeh, A., Ghorashi, M., Tatar, M., Yamini-
- 1239 Fard, F., Bergman, E., Jackson, J., & Parsons, B. (2010). The 2006 March 25 Fin
- 1240 earthquakes (Iran)—insights into the vertical extents of faulting in the Zagros Simply
- 1241 Folded Belt. *Geophysical Journal International*, 181(3), 1275–1291. 10.1111/j.1365-
- 1242 246X.2010.04601.x
- 1243 Rovida, A., Locati, M., Camassi, R., Lolli, B., & Gasperini, P. (2020). The Italian earthquake
- 1244 catalogue CPTI15. *Bulletin of Earthquake Engineering*, 18(7), 2953–2984.
- 1245 <https://doi.org/10.1007/s10518-020-00818-y>

- 1246 Ruff, L., & Kanamori, H. (1983). Seismic coupling and uncoupling at subduction zones.  
1247 *Tectonophysics*, 99(2), 99–117. 10.1016/0040-1951(83)90097-5
- 1248 Ruig, M. J. d. (1996). Extensional diapirism in the eastern Prebetic foldbelt, southeastern  
1249 Spain. *AAPG Memoir*, (65) <https://www.osti.gov/biblio/585188>
- 1250 Sàbat, F., Gelabert, B., Rodríguez-Perea, A., & Giménez, J. (2011). Geological structure  
1251 and evolution of Majorca: Implications for the origin of the Western Mediterranean.  
1252 *Tectonophysics*, 510(1), 217–238. 10.1016/j.tecto.2011.07.005
- 1253 Salas, R., Guimera, J., Mas, R., Martin-Closas, C., Melendez, A., & Alonso, A. (2001a).  
1254 Evolution of the Mesozoic Central Iberian Rift System and its Cainozoic inversion  
1255 (Iberian chain). *Mémoires Du Muséum National D'histoire Naturelle (1993)*, 186, 145–  
1256 186.
- 1257 Salas, R., Guimera, J., Mas, R., Martin-Closas, C., Melendez, A., & Alonso, A. (2001b).  
1258 Evolution of the Mesozoic Central Iberian Rift System and its Cainozoic inversion  
1259 (Iberian chain). *Mémoires Du Muséum National D'histoire Naturelle (1993)*, 186, 145–  
1260 186.
- 1261 Seranne, M. (1999). The Gulf of Lion continental margin (NW Mediterranean) revisited by  
1262 IBS: an overview. *Geological Society special publication* (pp. 15–36). The Geological  
1263 Society of London. 10.1144/GSL.SP.1999.156.01.03
- 1264 Serpelloni, E., Vannucci, G., Pondrelli, S., Argnani, A., Casula, G., Anzidei, M., Baldi, P., &  
1265 Gasperini, P. (2007). Kinematics of the Western Africa-Eurasia plate boundary from  
1266 focal mechanisms and GPS data. *Geophysical Journal International*, 169(3), 1180–  
1267 1200. 10.1111/j.1365-246X.2007.03367.x

- 1268 Sherkati, S., Molinaro, M., Frizon de Lamotte, D., & Letouzey, J. (2005). Detachment  
1269 folding in the Central and Eastern Zagros fold-belt (Iran): salt mobility, multiple  
1270 detachments and late basement control. *Journal of Structural Geology*, 27(9), 1680–  
1271 1696. 10.1016/j.jsg.2005.05.010
- 1272 Soler y José, R., Martínez del Olmo, W., Megías, A. G., & Abeger Monteagudo, J. A. (1983).  
1273 Rasgos básicos del neógeno del Mediterráneo español. *Mediterránea. Serie de*  
1274 *Estudios Geológicos*, 1, 71–82.
- 1275 Stampfli, G. M., & Hocker, C. F. W. (1989). Messinian palaeorelief from a 3-D seismic  
1276 survey in the Tarraco concession area (Spanish Mediterranean Sea). *Geologie En*  
1277 *Mijnbouw*, 68(2), 201–210.
- 1278 Stewart, S. A., Ruffell, A. H., & Harvey, M. J. (1997). Relationship between basement-linked  
1279 and gravity-driven fault systems in the UKCS salt basins. *Marine and Petroleum*  
1280 *Geology*, 14(5), 581–604. 10.1016/S0264-8172(97)00008-1
- 1281 Stich, D., Martín, R., & Morales, J. (2010). *Moment tensor inversion for Iberia-Maghreb*  
1282 *earthquakes 2005-2008*. Elsevier.
- 1283 Stich, D., Serpelloni, E., de Lis Mancilla, F., & Morales, J. (2006). Kinematics of the Iberia–  
1284 Maghreb plate contact from seismic moment tensors and GPS observations.  
1285 *Tectonophysics*, 426(3), 295–317. 10.1016/j.tecto.2006.08.004
- 1286 Stirling, M., Goded, T., Berryman, K., & Litchfield, N. (2013). Selection of earthquake  
1287 scaling relationships for seismic-hazard analysis. *Bulletin of the Seismological*  
1288 *Society of America*, 103(6), 2993–3011. 10.1785/0120130052

- 1289 Stirling, M., Rhoades, D., & Berryman, K. (2002). Comparison of earthquake scaling  
1290 relations derived from data of the instrumental and preinstrumental era. *Bulletin of*  
1291 *the Seismological Society of America*, 92(2), 812–830. 10.1785/0120000221
- 1292 Stock, C., & Smith, E. G. C. (2000). Evidence for different scaling of earthquake source  
1293 parameters for large earthquakes depending on faulting mechanism. *Geophysical*  
1294 *Journal International*, 143(1), 157–162. 10.1046/j.1365-246x.2000.00225.x
- 1295 Thorsen, C. E. (1963). Age of growth faulting in southeast Louisiana.
- 1296 Torné, M., Pascal, G., Buhl, P., Watts, A. B., & Mauffret, A. (1992). Crustal and velocity  
1297 structure of the Valencia trough (western Mediterranean), Part I. A combined  
1298 refraction/ wide-angle reflection and near-vertical reflection study. *Tectonophysics*,  
1299 203(1), 1–20. 10.1016/0040-1951(92)90212-O
- 1300 Tvedt, A. B. M., Rotevatn, A., Jackson, C. A. -, Fossen, H., & Gawthorpe, R. L. (2013).  
1301 Growth of normal faults in multilayer sequences: A 3D seismic case study from the  
1302 Egersund Basin, Norwegian North Sea. *Journal of Structural Geology*, 55, 1–20.  
1303 10.1016/j.jsg.2013.08.002
- 1304 Valoroso, L., Chiaraluce, L., Piccinini, D., Di Stefano, R., Schaff, D., & Waldhauser, F.  
1305 (2013). Radiography of a normal fault system by 64,000 high-precision earthquake  
1306 locations: The 2009 L’Aquila (central Italy) case study. *Journal of Geophysical*  
1307 *Research: Solid Earth*, 118(3), 1156–1176. <https://doi.org/10.1002/jgrb.50130>
- 1308 van Hinsbergen, D. J. J., Torsvik, T. H., Schmid, S. M., Mañenco, L. C., Maffione, M.,  
1309 Vissers, R. L. M., Gürer, D., & Spakman, W. (2020). Orogenic architecture of the  
1310 Mediterranean region and kinematic reconstruction of its tectonic evolution since the  
1311 Triassic. *Gondwana Research*, 81, 79–229. 10.1016/j.gr.2019.07.009

- 1312 van Hinsbergen, D. J. J., Vissers, R. L. M., & Spakman, W. (2014). Origin and consequences  
1313 of western Mediterranean subduction, rollback, and slab segmentation. *Tectonics*  
1314 (*Washington, D.C.*), 33(4), 393–419. 10.1002/2013TC003349
- 1315 Vargas, H., Gaspar-Escribano, J. M., López-Gómez, J., Van Wees, J., Cloetingh, S., de La  
1316 Horra, R., & Arche, A. (2009). A comparison of the Iberian and Ebro Basins during the  
1317 Permian and Triassic, eastern Spain: A quantitative subsidence modelling approach.  
1318 *Tectonophysics*, 474(1), 160–183. 10.1016/j.tecto.2008.06.005
- 1319 Verges, J., & Sabat, F. (1999). Constraints on the Neogene Mediterranean kinematic  
1320 evolution along a 1000 km transect from Iberia to Africa. *Geological Society special*  
1321 *publication* (pp. 63–80). The Geological Society of London.  
1322 10.1144/GSL.SP.1999.156.01.05
- 1323 Verges, J., & Fernandez, M. (2012). Tethys–Atlantic interaction along the Iberia–Africa  
1324 plate boundary: The Betic–Rif orogenic system. *Tectonophysics*, 579, 144–172.  
1325 10.1016/j.tecto.2012.08.032
- 1326 Wells, D. L., & Coppersmith, K. J. (1994). New empirical relationships among magnitude,  
1327 rupture length, rupture width, rupture area, and surface displacement. *Bulletin of the*  
1328 *Seismological Society of America*, 84(4), 974–1002.  
1329 <https://pubs.geoscienceworld.org/ssa/bssa/article/84/4/974/119792>
- 1330 Weng, H., & Yang, H. (2017). Seismogenic width controls aspect ratios of earthquake  
1331 ruptures. *Geophysical Research Letters*, 44(6), 2725–2732. 10.1002/2016gl072168
- 1332 Withjack, M. O., & Callaway, S. (2000). Active normal faulting beneath a salt layer; an  
1333 experimental study of deformation patterns in the cover sequence. *AAPG Bulletin*,  
1334 84(5), 627–651. 10.1306/C9EBCE73-1735-11D7-8645000102C1865D

- 1335 Withjack, M. O., Olson, J., & Peterson, E. (1990). Experimental models of extensional  
1336 forced folds. *AAPG Bulletin*, 74(7), 1038–1054. 10.1306/0C9B23FD-1710-11D7-  
1337 8645000102C1865D
- 1338 Yen, Y., & Ma, K. (2011a). Source-scaling relationship for M 4.6-8.9 earthquakes,  
1339 specifically for earthquakes in the collision zone of Taiwan. *Bulletin of the*  
1340 *Seismological Society of America*, 101(2), 464–481. 10.1785/0120100046
- 1341 Yen, Y., & Ma, K. (2011b). Source-scaling relationship for M 4.6-8.9 earthquakes,  
1342 specifically for earthquakes in the collision zone of Taiwan. *Bulletin of the*  
1343 *Seismological Society of America*, 101(2), 464–481. 10.1785/0120100046
- 1344 Zazo, C. (1979). El problema del límite Plio-Pleistoceno en el litoral S y SE de España.  
1345 *Trabajos N/Q*, 9, 65–72.
- 1346